Comparison of Wind Stress Algorithms, Datasets and Oceanic Power Input

by

Shaoyu YUAN

B.Sc., Ocean University of China, 2000

SUBMITTED TO THE JOINT PROGRAM IN PHYSICAL OCEANOGRAPHY - MASSACHUSETTS INSTITUTE OF TECHNOLOGY / WOODS HOLE OCEANOGRAPHIC INSTITUTION IN PARTIAL FULFILLMENT OF THE REQUIREMENTS FOR THE DEGREE OF

MASTER OF SCIENCE

AT THE

MASSACHUSETTS INSTITUTE OF TECHNOLOGY / WOODS HOLE OCEANOGRAPHIC INSTITUTION

Signature of Author .....
Joint Program in Physical Oceanography - Massachusetts Institute of Technology / Woods Hole Oceanographic Institution
December 10, 2008

Certified by .....
Carl Wunsch
Cecil and Ida Green Professor of Physical Oceanography
Thesis Supervisor

Accepted by .....
Raffaele Ferrari
Chair, Joint Committee for Physical Oceanography

In presenting this thesis in partial fulfillment of the requirements for an advanced degree at the Massachusetts Institute of Technology, I agree that the Library shall make it freely available for reference and study. I further agree that permission for extensive copying of this thesis for scholarly purposes may be granted by the head of my department or by his or her representatives. It is understood that copying or publication of this thesis for financial gain shall not be allowed without my written permission.

(Signature) .

Joint Program in Physical Oceanography - Massachusetts Institute of Technology / Woods Hole Oceanographic Institution

Massachusetts Institute of Technology / WOODS HOLE OCEANOGRAPHIC INSTITUTION
Cambridge, Massachusetts, USA

Date 12/12/08

Comparison of Wind Stress Algorithms, Datasets and Oceanic Power Input

by

Shaoyu YUAN

Submitted to the Joint Program in Physical Oceanography - Massachusetts Institute of Technology / Woods Hole Oceanographic Institution
on December 10, 2008, in partial fulfillment of the
requirements for the degree of
Master of Science

Abstract

If the ocean is in a statistically steady state, energy balance is a strong constraint, suggesting that the energy input into the world ocean is dissipated simultaneously at the same rate. Energy conservation is one of the most important principles in the natural world. However, the study of energy balance in the oceanic circulation has long been overlooked. Mink and Winch (1998) proposed that energy is needed to maintain the meridional overturning circulation and they also concluded that the wind energy input into the world ocean constitute the most important part. Since then, many estimates on the wind energy input have been given with a focus on different time and spatial scales.

It is well known that it is the air-sea momentum flux (wind stress) that actually drives the ocean circulation, especially the upper layer circulation. Due to the difficulties of directly measuring the wind stress, different algorithms were proposed to relate the wind stress with the wind velocity and other related atmospheric and oceanic variables. Different algorithms in fact produce quite different wind stresses, which may leads to spurious estimates in the wind energy input into the world ocean.

The thesis is organized as follows. In chapter 1, we try to understand the difference of four bulk algorithms, and conclude that different bulk algorithms may yield the wind energy input differences of 20%. Comparison of 4 different wind stress dataset were presented in Chapter 2. However, we do not determine which product is the best. In Chapter 3, a simple numerical experiment was executed and some preliminary estimate on the effects of introducing the wind stress dependence on the oceanic surface velocity were given. The ECCO data computation, however, does not produce the results as expected and some explanations are given.

Thesis Supervisor: Carl Wunsch

Title: Cecil and Ida Green Professor of Physical Oceanography

Chapter 1

Bulk Formulas

Knowledge of near-surface wind over the ocean is a key parameter for the investigation of many oceanographic, meteorological and climatic processes. Prior to the advent of spaceborne scatterometers, the temporal and spatial resolution and quality of ocean wind measurements (to a large extent from merchant ships) were far from satisfactory. The global wind field provided by the operational numerical weather prediction (NWP) has a better resolution, but the models are limited by our knowledge of the physical processes and the availability of data. Now the spaceborne scatterometers have demonstrated the capability for measuring the near surface wind velocity (both speed and direction) under clear and cloudy conditions, day and night.

However, wind velocity itself is not what matters. Dynamically it is the momentum flux at the air-sea interface (wind stress) that drives the oceanic general circulation. In the context of energy input, the dissipation of the ocean energy will be the same as the energy input into the ocean provided that the ocean is in a statistically steady state. Wind energy input into the ocean through the air-sea interface constitutes the most important part. The dot product of wind stress and oceanic surface current velocity defines the energy input rate. From the atmospheric aspect, a good quality wind stress dataset is essential for the quantification of the wind energy input.

Due to the difficulties of direct measurement of wind stress, wind stress is usually parametrized as $\tau = \rho_a C_D |U_a| \vec{U_a}$, where ρ_a is the atmospheric density, U_a is the atmospheric speed and C_D is called drag coefficient, which is a function of wind speed, atmospheric stratification, humidity and oceanic surface current, etc. However, the parametrizations of the drag coefficient have been debated over the past decades. Consequently, the uncertainties due to both the wind velocity and the parametrizations of the drag coefficient contribute to the uncertainties of wind stress and then the energy input into the ocean.

1.1 Bulk formula: theoretical background

The wind stress, exerted by the atmospheric flow over the sea surface, is essentially the momentum exchange between the atmosphere and ocean, denoted as $\tau_x = \rho_a \overline{u'w'}$ and $\tau_y = \rho_a \overline{v'w'}$. The Reynolds flux $\overline{w'x'}$ can be determined by measuring the time or space series of w', u' and v' and then calculating their mean product. This method, referred as covariance or eddy-correlation method, is the only way to directly measure the flux. Many other indirect approaches were also created due to the difficulties of direct measurement. For simplicity, different bulk algorithms, based on theories and observations, were proposed and have been widely used in most numerical models of air-sea interaction processes.

Since the momentum, sensible heat and latent heat fluxes couple together, it is not easy to separate one physical process from the other two. The latent and sensible heat flux will be discussed together with the momentum flux.

Wind stress, by definition, is the product of atmospheric density and the vertical turbulent flux of zonal momentum

$$\tau_x = \rho_a \overline{u'w'}, \tau_y = \rho_a \overline{v'w'}. \tag{1.1}$$

Note that this quantity can be measured at all altitudes.

In the atmosphere, at the bottom of the planetary boundary layer, a surface layer, whose depth depends on stability but is usually less than 10% of the total boundary layer depth, exists and it is maintained entirely by vertical momentum transfer by the turbulent eddies. Observations indicate that the surface momentum can be represented by a *bulk formula* (e.g. Brunke, *et al* 2003)

$$\overline{u'w'}_s = -C_D S(u - u_0); \ \overline{v'w'}_s = -C_D S(v - v_0). \tag{1.2}$$

where C_d is called the drag coefficient, u and v are the zonal and meridional wind speed, u_0 and v_0 are the ocean surface velocity. $S = \sqrt{(u-u_0)^2 + (v-v_0)^2 + w_g^2}$ is the near-surface wind speed with the inclusion of convective gustiness w_g ($S = \sqrt{(u-u_0)^2 + (v-v_0)^2}$ otherwise). w_g is defined as $w_g = \beta w_*$, where β is a coefficient and w_* is the convective velocity scale,

$$w_* = (-\frac{g}{\theta_v} \theta_{v*} u_* z_i)^{1/3}. \tag{1.3}$$

where θ_v is the virtual potential temperature, θ_{v*} is the scaling parameter for virtual potential temperature and z_i is the height of the atmospheric boundary layer.

The drag coefficient is a function of boundary layer stratification, specific humidity, the difference between the atmospheric and oceanic current velocity, and ocean waves, etc. Many different algorithms were proposed to parametrize C_D, to be discussed in more detail in the following section.

Monin-Obukhov similarity theory (Foken, 2006) states that in this layer

$$\frac{|\vec{u} - \vec{u}_0|}{u_*} = \frac{1}{\kappa}[ln(\frac{z}{z_0}) - \psi(\frac{z}{L})] \tag{1.4}$$

where z is the height above the ocean, z_0 is called aerodynamic roughness length, $\kappa = 0.4$ is the von Karman constant, $\vec{u}_0$ is the ocean surface velocity and u_* is the friction velocity, defined as

$$u_*^2 = \sqrt{|\overline{u'w'}^2 + \overline{v'w'}^2|} \tag{1.5}$$

L is the Monin-Obukhov length, the height at which mechanically produced (by vertical shear) turbulence is in balance with the dissipative effect of negative buoyancy,

$$L = -\frac{Tu_*^3}{\kappa g \overline{w'T_v'}} \tag{1.6}$$

where T is temperature and $T_v = T(1 + 0.61q)$ is the virtual temperature, and q is specific humidity; ψ is a universal function of of the dimensionless height $\xi = \frac{z}{L}$. ξ is called stability parameter. When L is negative with a small magnitude, ξ is negative with a large magnitude, which corresponds to large instability due to buoyancy. Positive values of ξ correspond to stable stratification. When the boundary layer is neutrally stable, L is infinitely large and the stability parameter $\xi = 0$. This function may vary with different algorithms.

The universal function ψ proposed by Paulson (1970) is widely accepted and gives a good fit to the data (Hogstrom, 1988)

$$\psi = 2ln[(x+1)/2] + ln[(x^2+1)/2] - 2tan^{-1}(x) + \pi/2 \tag{1.7}$$

where $x = (1 - 16\xi)^{0.25}$.

If the atmosphere is neutrally stable, $\xi = 0$ and $\psi_m(0) = 0$, and Eq. (1.4) reduces to

$$\frac{|\vec{u}_N - \vec{u}_0|}{u_*} = \frac{1}{\kappa} ln(\frac{z}{z_0}) \tag{1.8}$$

Combining Eqs. (1.1, 1.2, 1.5) yields the relation between the drag coefficient, the wind speed and the friction velocity,

$$C_D = \frac{u_*^2}{S|\vec{u}-\vec{u}_0|} = \frac{|\vec{u}-\vec{u}_0|}{S}\frac{C_{DN}}{[1-\kappa^{-1}C_{DN}^{1/2}\psi_m(\xi)]^2} \tag{1.9}$$

where $C_{DN} = \frac{\kappa^2}{(lnz/z_0)^2}$. If the convective gustiness is not included and $\xi = 0$, $C_D = C_{DN}$, so C_{DN} is usually called the neutral drag coefficient, where z is the reference height. Note that *here* C_{DN} is defined to be the function of the same z_0 as used in C_D. From Eq. (1.9), the drag coefficient C_d is technically determined with the knowledge of z_0 and ξ. Notice that

$$\rho_a C_{ND}(u_N - u_0)^2 = \rho_a \frac{\kappa^2}{ln(z/z_0)^2}\frac{u_*^2}{\kappa^2} ln(z/z_0)^2 = \rho_a u_*^2 \tag{1.10}$$

It is readily seen that

$$\tau = \rho_a C_D S(u-u_0)^2 = \rho_a C_{ND}(u_N - u_0)^2 \tag{1.11}$$

Traditionally, the oceanic surface current velocity is neglected considering the fact usually $u_0 \ll u$. However, recent studies show ignoring the ocean current dependence in the wind stress significantly increases the calculated global energy input to the oceanic general circulation. The removal of the stress dependence on the ocean surface current artificially removes the oceanic damping over the regions of strong currents.

Latent and sensible heat flux

The latent and sensible heat flux are defined respectively as

$$E = \rho_a L_v \overline{w'q'} \tag{1.12}$$

$$H = \rho_a C_p \overline{w'\theta'} \tag{1.13}$$

where L_v is the latent heat of evaporation, C_p the specific heat at constant pressure, q the specific humidity and θ the potential temperature. Based on the scaling parameter for wind or friction u_*, the scaling parameters for humidity q_* and potential temperature θ_* are defined as

$$q_* = -\frac{\overline{w'q'}}{u_*} \tag{1.14}$$

$$\theta_* = -\frac{\overline{w'\theta'}}{u_*} \tag{1.15}$$

By defining turbulent exchange coefficients $C_E = -\frac{u_* q_*}{S(q_s - q_a)}$, and $C_H = -\frac{u_* \theta_*}{S(\theta_s - \theta_a)}$ (q_s and q_a are the surface and near surface atmospheric specific humidities; θ_s and θ_a are the surface and near surface air potential temperatures), the turbulent fluxes are directly related to the meteorological measurements

$$E = \rho_a L_v C_E S(q_s - q_a) \tag{1.16}$$

$$H = \rho_a C_p C_H S(\theta_s - \theta_a) \tag{1.17}$$

In general, the coefficients C_d, C_H and C_E are functions of wind speed, atmospheric stability, ocean current, and waves, etc.

Monin-Obukhov similarity theory also states that for potential temperature and specific humidity

$$\frac{\theta - \theta_0}{\theta_*} = \frac{1}{\kappa}[ln(\frac{z}{z_{0\theta}}) - \psi_\theta(\frac{z}{L})] \tag{1.18}$$

$$\frac{q - q_0}{q_*} = \frac{1}{\kappa}[ln(\frac{z}{z_{0q}}) - \psi_q(\frac{z}{L})] \tag{1.19}$$

where $z_{0\theta}$ and z_{0q} are the roughness length corresponding to potential temperature and specific humidity; ψ_θ and ψ_p are also universal functions (Paulson, 1970).

Atmospheric winds are essential for reliable computations of C_D, C_E and C_H. However, the satellite-derived wind speeds are equivalent neutral wind (ENW) speeds instead of the actual winds (Risien and Chelton, 2008). Up to now, the definition of ENW is somewhat ambiguous. In general, there are two definitions. The equivalent neutral wind speed is commonly defined as the mean wind speed that would exist under the neutral atmospheric stratification. Neutral drag coefficients and roughness lengths can be determined according to this definition.

If convective gustiness is neglected, Eq. (1.9) is written as

$$\kappa C_d^{-1/2} = ln\frac{z}{z_0} - \psi_m \tag{1.20}$$

If one considers the case of neutral stratifications where $\psi_m = 0$, the drag coefficient and roughness length might be defined as C_{dN} and z_{0N}, respectively, where the subscript N indicates

neutral stratification. Now Eq. (1.20) reduces to

$$\kappa C_{dN}^{-1/2} = ln\frac{z}{z_{0N}} \tag{1.21}$$

The relation between C_d and C_{dN} can be obtained from combining Eqs. (1.20, 1.21)

$$C_d = (C_{dN}^{-1/2} - \frac{\psi_m}{\kappa} + \frac{1}{\kappa} ln\frac{z_{0N}}{z_0})^{-2} \tag{1.22}$$

In interpreting Eq (1.22), the relation between the drag coefficient, the neutral drag coefficient, the roughness and neutral roughness, it must be remembered that these parameters refer to the same wind speed at a reference level. The corresponding wind stresses may vary due to different stratifications, and so do the roughness lengths.

As is commonly known that the scatterometers measure surface stress instead of the surface wind itself (refer to Chapter 2 for details). The observed radar backscatter is calibrated to equivalent neutral wind speed according to the following definition. Roughness length and stability functions consistent with the atmospheric observations are used to calculate the ENW with the atmospheric stratifications term in the modified log-wind profile set to zero. With this definition, the conversion of wind stress to the ENW is straightforward regardless of the atmospheric conditions at the time of measurement (more details below), and vice versa (Risien and Chelton, 2008).

1.2 Bulk Algorithms: Comparison

Because wind stress, sensible and latent heat flux couple together, they are computed simultaneously in all bulk algorithms. Eqs. (1.4, 1.6, 1.18, 1.19) can be rewritten as

$$u_* = u_*(z_0, \zeta)$$

$$\zeta = \zeta(u_*, \theta_*, q_*)$$

$$\theta_* = \theta_*(z_{0\theta}, \zeta)$$

$$q_* = q_*(z_{0q}, \zeta)$$

Now there are four equations with seven variables (u_*, θ_*, q_*, z_0, $z_{0\theta}$, z_q and ζ). Three more equations are needed to get the drag coefficients and the corresponding fluxes.

Bulk algorithms differ in how they parametrize the exchange coefficients and the representation of roughness lengths for wind, temperature and humidity to provide three more equations. Here several algorithms, which are generally believed to be useful, are chosen to study the drag coefficient difference and the energy input difference associated with different algorithms.

2.1 ECMWF Algorithm (ECMWF)

The algorithms in the ECMWF forecast model (Beljaars 1994) uses the Monin-Obukhov similarity theory. In the computation of scalar wind speed, the convective gustiness is included. The roughness lengths for momentum, heat and moisture are parametrized as

$$z_0 = \frac{0.018u_*^2}{g} + \frac{0.65 \times 10^{-6}}{u_*} \tag{1.23}$$

$$z_{0t} = \frac{6 \times 10^{-6}}{u_*} \; and \; z_{0q} = \frac{9.3 \times 10^{-6}}{u_*} \tag{1.24}$$

The surface humidity over salt water is usually depressed by around 2% compared to that of pure water. However, this effect is not included in this algorithm. It might be an essential factor in the computation of the surface latent heat flux under strong wind conditions.

With proper initial conditions (u_*, θ_*, q_*, z_0 and ζ), a few iterations are all that is necessary to yield the converged u_*, θ_*, q_*, z_0 and ζ associated with the given atmospheric speed, stratifications and specific humidity. The corresponding wind stress, latent and sensible heat flux can be calculated accordingly.

2.2 University of Arizona Algorithm (UA)

Zeng, *et al.* (1998) developed a new bulk aerodynamic algorithm. It is similar to the ECMWF algorithm with some modifications. It differs slightly from the ECMWF algorithm in the parametrization of roughness length for momentum flux

$$z_0 = \frac{0.013u_*^2}{g} + \frac{0.11\nu}{u_*} \tag{1.25}$$

where $g = 9.81N/m^2$ and ν is air kinematic viscosity.

However, parametrizing the roughness lengths for heat and moisture is quite different (Brutsaert, 1982)

$$ln(\frac{z_0}{z_{0t}}) = ln(\frac{z_0}{z_{0q}}) = 2.67Re_*^{1/4} - 2.57 \tag{1.26}$$

where $Re = u_* z_0/\nu$ is the roughness Reynolds number and ν the kinematic viscosity of air. The salinity effect coefficient 0.98 was applied in this algorithm,

$$q_s = 0.98 q_{sat}(T_s) \tag{1.27}$$

In the computation of the drag coefficient and corresponding wind stress, latent and sensible heat flux, only a few iterations, with proper initial guess, are needed to produce the results because the atmospheric layer is usually very close to neutrally stable (Zeng, *et al.* 1998).

2.3 Liu and Tang Algorithm (LT96)

The LT96 algorithm is the one usually used to convert the *in situ* observed winds to the neutral-stability winds for the purpose of calibration of the scatterometer data produced by an *inverse transfer function* (this will be discussed in Chapter 2).

LT96 proposed that

$$z_0 = \frac{0.011 u_*^2}{g} + \frac{0.11\nu}{u_*} \tag{1.28}$$

$$\theta_* = \frac{h_t u_*}{\nu}$$

$$q_* = \frac{h_q u_*}{\nu}$$

where h_t and h_q are the height of the potential temperature and specific humidity sensors.

If the neutral winds whose z_0 and ξ are consistent with the observations are provided (e.g. satellite derived ENW), it is straightforward to compute the stress. Combining Eqs. (1.8, 1.23,1.25,1.28) produces z_0 and u_*. The corresponding stress and neutral drag coefficient are then computed according to the definition.

2.4 Large and Yeager 2004 (LY04) Algorithm

The LY04 algorithm is widely used in oceanic models including the MITgcm (Marshall, 1997). The concept of equivalent neutral wind is used in this algorithm. Based on the fact that quite a few field experiments show that the neutral drag coefficient tends to be a function of only wind speed at a reference level (e.g.$10m$) under the neutrally stable conditions. The neutral drag coefficient C_{DN}, at $10m$ above the ocean, is usually written as

$$C_{DN} = (aU_{10N}^{-1} + b + cU_{10N}) \times 10^{-3} \tag{1.29}$$

where a, b and c are generally functions of u_{10N} and determined by the data. For the LY algorithm, $a = 2.70$, $b = 0.142$, and $c = 0.76$. When U_{10N} is infinitely small, C_{DN} is infinitely large, so a minimum U_{min} is usually set in the computation to avoid the singularity.

The transfer coefficients for evaporation, C_E, and sensible heat, C_H are given as follows

$$1000C_E = 34.6\sqrt{C_D} \tag{1.30}$$

$$1000C_H = \begin{cases} 18.0\sqrt{C_D} & \text{if stable } \zeta > 0 \\ 32.7\sqrt{C_D} & \text{if unstable } \zeta \leq 0 \end{cases} \tag{1.31}$$

Instead of parametrizing the roughness lengths, the LY04 parametrized the neutral drag coefficient directly as functions of neutral wind speed. In contrast to other algorithms, while doing the iterations, the potential temperature and specific humidity data have to be shifted to $10m$ above the ocean to use the above parametrizations if the given data are not on that level. The details will not be discussed here.

The LY04 algorithm is not alone; there are quite a few similar parametrizations along this track. For example, based on Large and Pond (1982), Dittmer (1977) and Schacher (1981), Trenberth, *etc* (1989) proposed that

$$10^3 C_d = \begin{cases} 0.49 + 0.065U_{10N} & \text{if } U_{10N} > 10ms^{-1} \\ 1.14 & \text{if } 3 \leq U_{10N} \leq 10ms^{-1} \\ 0.62 + 1.56U_{10N}^{-1} & \text{if } U_{10N} \leq 3ms^{-1} \end{cases}$$

As in other algorithms, the use of these algorithms also require the knowledge of the wind profile ψ_m, and necessary iterations to reach converged solutions.

As discussed in the introduction, the wind stress essentially depends on the difference between the atmospheric speed and the oceanic surface speed instead of the atmospheric speed itself, so does the drag coefficient. Initially, most of the bulk algorithms exclude this dependence. However, this can be introduced easily by replacing the atmospheric speed with the difference.

Different algorithms produce different drag coefficients and wind stress. Because the atmosphere is nearly neutrally stable, it is interesting to see the difference under this circumstance. In this example, the wind stress drag coefficient and the coefficients for the sensible and latent

flux decouple. For the ECMWF, UA and LT96 algorithms, two equations for u_* and z_0 are used to yield C_{DN} as a function of u_{10N}. For the LY04 algorithm, it is even easier because C_{DN} is directly parametrized as a function of u_{10N}.

If the boundary layer is neutrally stable, the LT96 algorithm, for example, is reduced to

$$z_0 = \frac{0.011u_*^2}{g} + \frac{0.11\nu}{u_*}$$

$$u_* = \frac{\kappa U_N}{ln(\frac{z}{z_0})}$$

where U_N is the atmospheric neutral winds. With proper initial guess of z_0 and u_*, a few iterations yield the converged z_0 and u_*. The corresponding wind stress and drag coefficient are readily available. If the wind stress is available, u_* can be computed by definition. the computation of z_0 and U_N is straightforward using the two equations above.

Fig. 1.1 display the drag coefficients as a function of wind speed under the neutral-stability conditions for the four algorithms. The four curves have similar patterns. A minimum value is found for all four. The values of U_0 for the minimum are mathematically computable, which are 1.86, 2.72, 2.89 and 5.95 for ECMWF, UA, LT96 and LY04 algorithms, respectively. These values differ significantly due to different parametrizations. It is interesting that when U tends to zero, the LY04 drag coefficient tends to be infinitely large, while other coefficients seem to reach constant values (little is unknown).

The LT96 and UA algorithms are very close at low wind speed ($U < 3$); while $U < 3$, LT96 values are a little smaller than UA values. For the LY04 algorithm, the drag coefficient C_{DN} has a minimum at $U_0 = 5.95m/s$. C_{DN} increases with the increase of U when $U > U_0$; C_{DN} decreases when $U < U_0$. C_{DN} tends to infinity when U approaches 0. Because of this behavior, the drag coefficient generated by LY04 is significantly different from any other algorithm under low wind speed conditions (e.g. $U < 1$). In fact, the algorithm itself (at least in MITgcm) also sets a minimum wind speed of $U = 0.1$ to avoid super large values of C_d.

At the range of $5 < U < 20$, $C_{D(ECMWF)} > C_{D(UA)} > C_{D(LY96)} > C_{D(LY04)}$ and the average values are $(1.59, 1.47, 1.41, 1.34) \times 10^{-3}$. The ECMWF is around 19% larger than the LY04 coefficient. It is expected that the produced ECMWF stress is roughly 19% stronger than the LY04 stress.

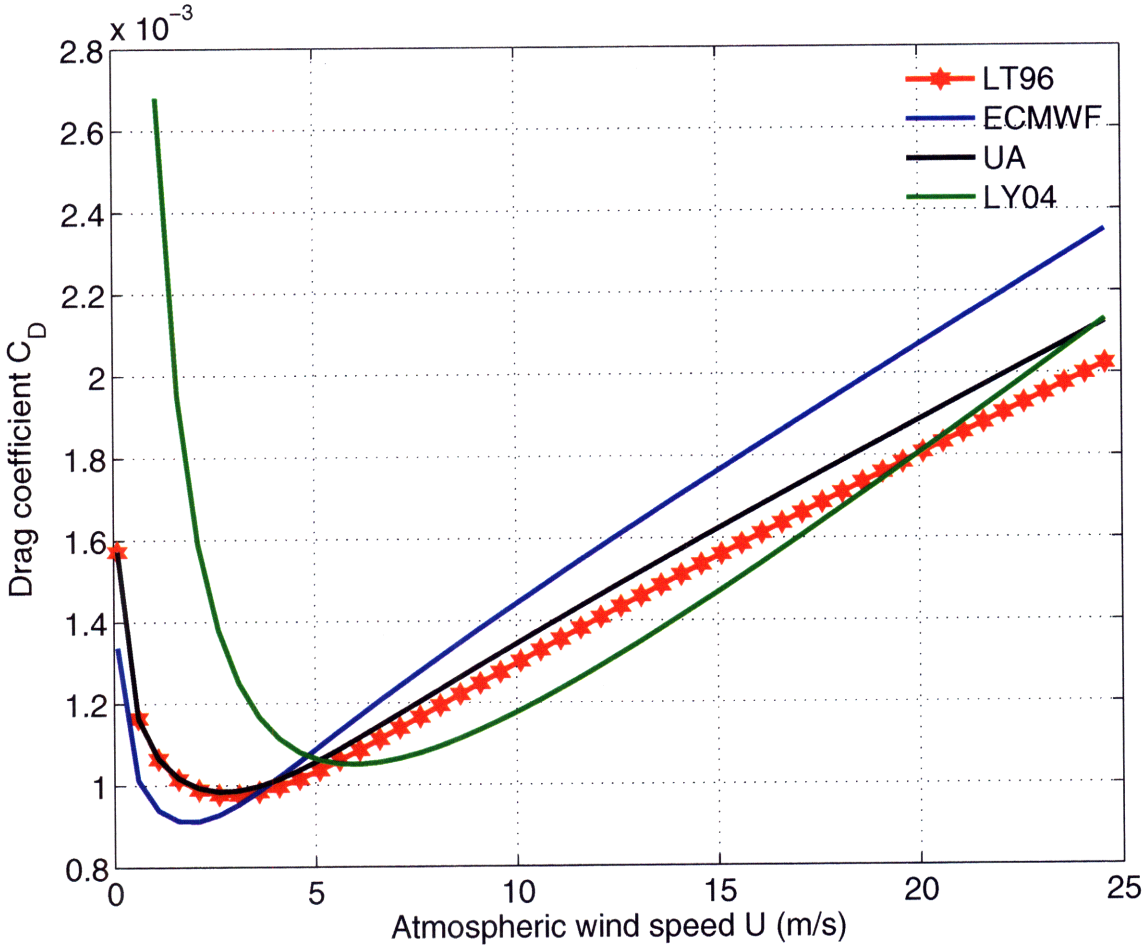

Figure 1.1: Neutral drag coefficient as a function of neutral wind speed (m/s). The neutral wind speed can be described either as the atmospheric neutral speed or the difference between the atmospheric and oceanic surface speed.

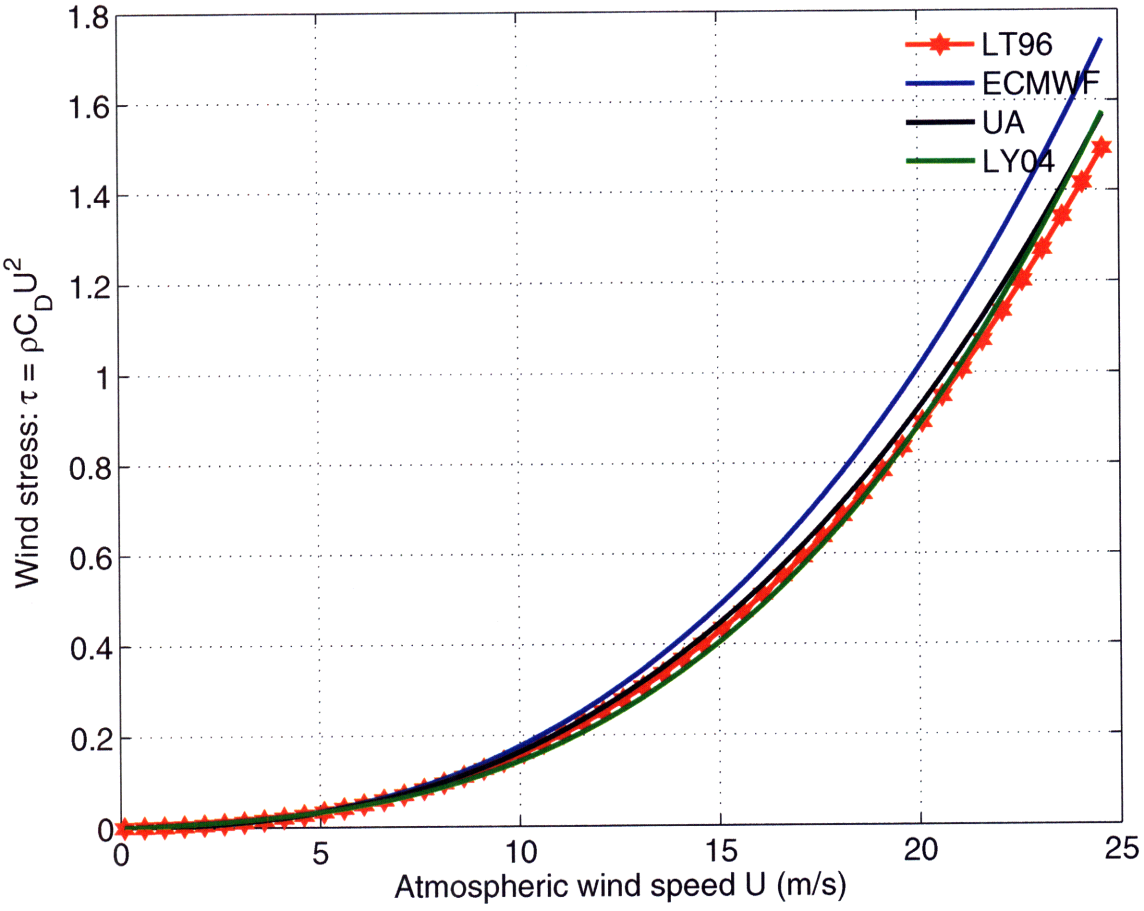

Figure 1.2: Wind stress as a function of neutral wind speed (m/s)

Fig. 1.2 shows the corresponding wind stress as a function U. In contrast to the C_d variation, the wind stress τ increases monotonically with ENW. Since the equivalent neutral wind removes the stability effects, the stronger the ENW, the larger the stress. Apparently between $10 < u < 20m/s$, $\tau_{ECMWF} > \tau_{UA} > \tau_{LT} > \tau_{LY04}$. The wind stress approaches zero when U tends to zero as expected, and the LY algorithm decreases much more slowly than the other algorithms.

Based on the same wind velocity data, different algorithms produce different drag coefficients and consequently different wind stresses. The neutral-stability winds are the best wind (velocity) data available (Risien and Chelton, 2008). However, the converted wind stress from the wind data can be quite different if different bulk algorithms are used. It is still questionable to say how good the satellite wind stress data are without understanding which bulk algorithm is better. For other wind stress data, different wind velocity data may be used in the calculation and it is too early to tell the difference without a direct comparison. In the next Chapter, four different datasets will be compared.

Chapter 2

Comparison of Different Wind Datasets

As discussed in the Chapter 1, wind stress plays a dominant role in driving the oceanic circulation. More than half of the energy necessary to sustain the meridional circulation is from the wind work on the ocean surface current (Munk and Wunsch, 1998; Wunsch and Ferrari, 2004). The dot product of wind stress and surface current produces the energy input to the ocean, which may be an important parameter which controls the meridional circulation. However, although many different wind stress datasets are available and their key features are similar, they differ in many aspects. In this chapter, four different datasets, including the stress datasets from Scatterometer Climatology of Ocean Winds (SCOW), National Centers for Environmental Prediction (NCEP), European Centre for Medium-Range Weather Forecasts (ECMWF), and Estimating the Circulation & Climate of the Ocean (ECCO), are compared in detail.

2.1 Description of different datasets

2.1.1 SCOW Datasets

The QuikSCAT mission was proposed to measure sea-surface wind speed and direction under all weather and cloud conditions over the world ocean, and it was initiated as a "quick recovery" mission to help reduce the ocean-wind vector data gap created by the loss of the NASA Scatterometer (NSCAT) on the Japanese Advanced Earth Observing Satellite (ADEOS), which ceased functioning when ADEOS failed on June 30, 1997.

Spaceborne scatterometer measurements are highly indirect. Scatterometers transmit microwave pulses to the ocean surface and measure the backscattered power received from the instrument, from which the normalized radar cross section of the sea surface (σ_0) can be calculated. σ_0 is calculated from the basic radar equation (Naderi, *et al.*, 1991). The received power is the fundamental measurement; it (also σ_0) is determined by the radar frequency (v), polar-

ization (p), incident angle (θ), and the surface geometry (essentially surface wind speed vector V): $\sigma_0 = G(V, \theta, v, p)$, where G is known as a *geophysical model function* (GMF). The model function should be derivable from theory alone in principle. However, because of the inadequacy of our understanding of both the relationship between the wind and the surface geometry, and the interaction between electromagnetic radiation and the sea surface, empirical models were established to relate σ_0 and the surface wind. The surface wind velocity (both speed and direction) can be retrieved according to the *inverse transfer function*: $V = g(\sigma_0, \theta, v, p)$. Because g is usually a multivalued function, several measurements of σ_0 from different azimuthal angles are used to uniquely estimate the wind speed.

The estimated wind speed is actually the equivalent neutral-stability wind (ENW) at the height of 10m above the sea surface. ENW is the wind that would exist if the atmosphere were neutrally stable. The ENW can be converted from actual wind measurements easily using the Liu and Tang (1995) algorithm if the simultaneous measurements of air and sea surface temperature (stratification) are available. Thus a much larger database of ENW is available than that of direct measurements of stress for the purpose of calibration.

The scatterometer is essentially a stress measuring instrument (Risien and Chelton, 2008). However, because the database of direct measurements of stress for calibration purposes is inadequate, the *geophysical model function* is constructed as a function of wind speed vector instead of wind stress vector and the radar backscatter is calibrated to the ENW at a height of 10 m above the sea surface. To the extent that the atmospheric boundary layer is near neutrally stable over most of the world ocean, ENW seldom differs by more than a few tenths of a meter per second from the corresponding actual wind. At times and locations of significant deviation from neutral stability, the two will differ.

Conversion of ENW to wind stress using bulk aerodynamic algorithms is straightforward, regardless of the actual stability at the time of measurement, since roughness length and stability functions corresponding to ENW are consistent with observations (Liu and Tang 1996).

Traditionally in the bulk algorithms, the wind stress is parametrized only as a function of atmospheric speed at a reference level ($\tau = \rho_a C_d u_a^2$). However, recent studies indicate that stress actually depends on the difference between the surface wind and current speed ($\tau = \rho_a C_d (u_a - u_0)^2$) (Duhaut and Straub, 2006). What scatterometers indirectly measure is

in fact the surface wind stress instead of the wind itself. Recent studies (Chelton, *et al.*, 2004; Risien and Chelton, 2008) reveal that many smaller scale ocean current features appear in the satellited derived date, especially when derivatives are considered.

2.1.2 NCEP Datasets

The NCEP in cooperation with National Center for Atmospheric Research (NCAR) has been using a frozen state-of-the-art global data assimilation system and a database as complete as possible to produce a retroactive record of more than 50 years of global analyses of atmospheric fields in support of the rewarch and climate monitoring communities. The recovery of land surface, ship, aircraft, satellite, and other data are involved. The analyses are produced by combining observations derived from the global observation network with the short term forecast. The details can be found in Kalnay *et al.* 1996 and Kistler *et al.* 2000.

Operational NCEP analyses are based on a three-dimensional variational (3D Var) system; the underlying spectral model is run at a T170 resolution (about 1°) and exhibits 42 sigma levels between the ground and 2 hPa. Wind stress is one of its outputs.

2.1.3 ECMWF Datasets

The ECMWF re-analysis project is in two phases. The first, ERA-15 generated re-analyses from December 1978 to February 1994. The second, ERA-40, begins in 1957 (the International Geophysical Year). ECMWF analyses are produced by a four-dimensional variational (4D Var) data assimilation system, using a T511 spectral model (about 0.4° resolution); the 60 hybrid model levels cover the atmosphere from the ground to 0.1 hPa.

2.1.4 ECCO Datasets

As part of the World Ocean Circulation Experiment (WOCE), ECCO was established in 1998 as a consortium of Scripps Institute of Oceanography (SIO), Massaschusetts Institute of Technology (MIT) and Jet Propulsion Laboratory (JPL) in an effort to combine a general circulation model (GCM) with diverse observations to produce a quantitative depiction of the time-evolving global ocean state. In contrast to meteorological "data assimilation", driven by the compelling

need to forecast the weather, the dominant problem in oceanography at present is to understand how the system works due to the difficulties of obtaining enough observations. "State estimate" is the term used by oceanographers. Automatic differentiation (AD) tools were applied to generate tangent linear and adjoint code for ocean circulation and climate studies. The system has been used to study problems of ocean state estimation. The MIT general circulation model (GCM) outputs and oceanic observations have been combined to generate the estimate (Wunsch and Heimbach, 2007). Essentially, the ECCO data can be considered the sum of the model output and the corresponding adjustment.

ECCO system uses NCEP wind data to drive the model. Consequently, the ECCO stress data are actually the adjusted NCEP data.

2.2 Data Comparison

Four different datasets are compared in this section. The SCOW data are the 8-year monthly mean data ranging from September 1999 to August 2007 and they are on a 0.25° latitude by 0.25° longitude grid spanning from 0.125°E to 0.125°W and 69.875°S and 69.875°N. The NCEP and ECCO data are obtained from the same time range and the spatial resolution is 1° by 1°; the ECMWF data are generated from 7-year data from 2000 to 2006 because the 2007 data are not available.

Although there are also some problems with the scatterometer data, summarized at the end of the chapter, they are still considered the best available wind data (Chelton and Freilich, 2005; Risien and Chelton, 2008). The comparison is based on the differences between different data with SCOW data.

2.1 SCOW and NCEP

All the features known to exist in the surface stress are prominent in both the SCOW and NCEP stress fields as displayed in the upper and middle panels in Fig. 2.1. Located in the tropics between about 30°N and 30°S are the trade winds. The Intertropical Convergence Zone (ITCZ), also known to mariners as the doldrums, is located north of the equator. Year-round westerlies prevail in the middle latitudes (between 30° and 60°). The westerlies can be particularly strong, especially in the southern hemisphere, where there is less land in the middle

latitudes to cause friction and slow the winds down. The Indian Ocean monsoon completely reverses its direction from January to July and vice versa.

The NCEP data are on $1° \times 1°$ grid and they were bilinearly interpolated to the SCOW $0.25° \times 0.25°$ grid for the purpose of comparison.

Although the major structures in the NECP wind stress are similar to those in the SCOW data, the magnitude difference between NCEP and SCOW data, displayed in the lower panels (Fig. 2.1), shows a few easily visible regions where there exist significant differences. In the Southern Ocean, the NCEP stress magnitudes are generally 35% stronger than SCOW stress. The greatest differences occur in the Indian Ocean section of the Southern Ocean. It is believed that the inadaquacy of in situ ship observations leads to the deviation of model states from the SCOW states in the Southern Ocean. An interesting exception is that there are patches of regions in the South Indian Ocean along the meandering Agulhas Return Current (ARC) between 40 and 45°S and 25 and 70°E where the the SCOW wind stress magnitudes are stronger than the NCEP wind stress fields, consistent with what O'Neil et al., (2003, 2005) described: the wind stress is intensified over warm-core eddies and decreased over cold-core eddies shed from the ARC. The higher resolution of SCOW data make it possible to resolve the features producted by the coupling between surface winds and meso-scale oceanic eddies. The unstable marine atmospheric boundary layer created by the air-sea temperature difference and secondary circulations perpendicular to SST fronts induced by the temperature constrasts associated with the SST fronts are the mechanisms that contribute to the wind variations over SST fronts. The weakness of the NCEP stress in the eastern tropical Pacific (cold tongue region) may also be attributed to the coupling between SST and surface winds.

In January, to the northwest of the north Pacific, the NCEP stress is weaker than the SCOW stress; to the northeast the NCEP stress is stronger; the NCEP stress is stronger in North Atlantic. In northern winter, the NCEP stress is significantly stronger than the SCOW stress in the Labardor sea; however, they differ only slightly in summer.

In the oceanic interior, a basic balance is the Sverdrup relation, which is the balance between the planetary vorticity and the wind stress curl (vertical vorticity). Wind stress curl also generates Rossby waves, which, with free Rossby waves, play a critical role in the oceanic dynamics. A good quantification of wind stress curl fields is clearly important. The upper and

middle panels in Fig. 2.2 display the wind stress curl fields for both SCOW and NCEP data and their differences (bottom panels). The two maps share similar patterns: in the northern subpolar gyre, the curl is generally positive; in the northern subtropical gyre, it is negative. The band of positive curl around 8 to 10°N coincides with the location of shallowest thermocline in the tropical Pacific (Wang, 1999). From 25 to 45°S, the wind curl is broadly positive, while south of that in the Southern Ocean, the wind curl is negative. In the Northern Hemisphere, the wind stress curl is much stronger in boreal winter than that in summer; while in the Southern Hemisphere, the wind stress curl becomes only slightly stronger from January to July as displayed in Fig. 2.2.

Although sharing many similar features, the SCOW and NCEP differ in some aspects. Compare the top and middle panels, the NCEP wind stress curl is more like a smoothed version of the SCOW stress curl. The SCOW data clearly show some fine structures associated with the air-sea interaction. For instance, right above the Gulf Stream in the Atlantic, a very thin and long line of positive curl distinguishes itself from the surrounding negative curl. It is not possible to observe such small-scale features in coarse resolution datasets. As shown in the bottom panels of Fig. 2.2 , in the boreal winter, north of 35°N and south of 40°S, the two curls differ significantly. However, there is no readily visible regions where the NCEP data are uniformly stronger or weaker.

The wind stress divergence has no dynamical effects on the ocean current, but it is an indicator of the coupling between the ocean and atmosphere. For example, the interaction between SST and wind is clearly visible in the divergence maps. As seen in Fig. 2.3, alternating patches of divergence and convergence occur in the Pacific and northwest Atlantic and all over the Southern Ocean. These regions are full of strong eddies, warm or cold. Right above the warm eddies, the wind stress is intensified; while over the cold eddies, the wind stress is reduced. Divergence/convergence is developed while the wind is from cold/warm to warm/cold eddies. The NCEP data do not resolve such small-scale signals. The parallel bands of strong divergence and convergence in the tropical Pacific are attributed to the coupling of wind stress and the SST fronts on both sides of the equatorial cold tongues too. Different from the meso-scale eddies, the cold tongues have much larger scale and the divergence and convergence are distinguishable on both SCOW and NCEP maps.

The magnitude difference is shown in the bottom panel of Fig. 2.3. Not surprisingly, the NCEP divergence is broadly smaller than the SCOW divergence in the eddy-rich regions. For some unclear reason, the NCEP divergence is much stronger in the Labrador sea.

The longitudinally averaged zonal stress for SCOW, NCEP, ECMWF and SCOW is shown in Fig. 2.4. As described above, in the Southern Ocean, the SCOW is significantly weaker than NCEP stress, while the difference in the region from 40°S to 35°N is small. North of 35°N, they differ.

2.2 SCOW and ECMWF

The ECMWF stress (EA) maps are displayed in Fig. 2.5.They share similar features with SCOW maps. The magnitude difference as shown in the bottom panels of Fig. 2.5 has similar features with the difference between NCEP and SCOW datasets, which indicates that the NCEP and EA data are quite close as shown in the zonally averaged zonal stress. In the Southern Ocean, the EA magnitudes are even a little stronger than NCEP data. Not surprisingly, the EA magnitudes are much larger in the Southern Ocean. In the north Pacific between 160°E to 130°W and 25°N to 35°N, EA stress is much stronger than the SCOW stress. It is noticed that the EA stress is weaker than NCEP stress to the northwest in the north Pacific, as shown in Fig. 2.6, the magnitude differences between NCEP and EA stress. In other regions, the differences are small.

The middle and bottom panels in Fig. 2.5 show the magnitude difference of wind curl and divergence. These maps are very similar to those differences between NCEP and SCOW, indicating that the NCEP and EA data do not differ qualitatively. NCEP and EA data differ in details, but direct comparison of NCEP and EA data does not show significant differences with the only exception that EA divergence is a little stronger in the eastern tropical Pacific

2.3 SCOW and ECCO

According to the definition, ECCO = NCEP + adjustment. It is interesting to know what the adjustment is. However, since the SCOW data are considered the best available data, the comparison is still based on SCOW data.

It is interesting that Fig. 2.4 shows that the adjustment tends to increase the magnitudes of the zonal stress at local maxima, although the NCEP data tend to be large already compared to the SCOW data.

Fig. 2.8 shows the wind stress magnitude, curl and divergence maps for the ECCO data. Although sharing similar patterns, ECCO data clearly have a larger magnitude. Although the ECCO data are on a 1° by 1° grid, they show much more fine-scale features in the curl and divergence maps. In the subpolar gyres of north Pacific and Atlantic, large patches of negative curls are visible, which are not found in the NCEP maps.

The difference between ECCO and SCOW data is displayed in Fig. 2.9. The magnitude difference shows strong seasonal dependence as shown in the top panels. In January, the two are close in the tropical Indian ocean; while in July, the ECCO becomes dramatically weaker. Also in the north subpolar Pacific and Atlantic Ocean, the ECCO stress is much stronger than SCOW stress in July; while in January, the difference is not that large. There are more regions clearly visible in the maps. However, the curl and divergence maps do not show evident seasonal dependence.

2.3 Summary

In this charter, with the assumption that SCOW data are the best, all the maps are based on the comparison with SCOW data, NCEP, EA or ECCO data.

The coupling of the wind stress with oceanic SST in the vicinity of strong SST fronts is an important air-sea process. The availability of the high resolution SCOW data provides the possibility to observe the oceanic signals from the wind stress. As discussed above, this contributes most to the divergence difference maps.

The zonal stresses for ECCO, SCOW, NCEP and EA averaged over longitude are displayed in Fig. 2.4. Among these stresses, ECCO stress has the maximum magnitude, while SCOW magnitude is the smallest. The SCOW, NCEP and EA data match quite well from 40°S to 40°N. The disagreement becomes significant in the westerlies in both hemisphere and the disparity is especially large in the Southern Ocean.

Among these products, ECCO data are the only one which are produced by oceanographers instead of meteorologists. The divergence and curl maps surprisingly show some small scale structures. Whether the small scale features are physical or not is an interesting question. Here we do not investigate much, but a simple power density spectrum analysis is performed for the

divergence map in January along 57.63°S, where there is no land along this line, as shown in Fig. 2.10. It is surprised to see that there are 4 minima, corresponding to $2R_L$, R_L, $\frac{2}{3}R_L$, and $\frac{1}{2}R_L$ from left to right, respectively, where $R_L = 2\pi Rcos(57.62)/360$=59.54km, and R = 6371km, the Earth Radius. This coincidence is a strong indication that the smaller features may be nonphysical. It may be associated with model smoothing configurations. Further investigation is needed.

Although it is believed that the SCOW data are the best available data, there are problems and the data can also be contaminated by quite a few factors:

1. Rain effects. The data can be contaminated by rain in two ways: a. in the presence of significant rain, the microwave radiation can be scattered or even absorbed by raindrops in the atmosphere. The microwave propagation through the atmosphere differs significantly from that in nonraining conditions; b. the centimetric roughness caused by the raindrops hitting the sea surface is not correlated with what is generated by the wind stress. Different algorithms were developed to detect rains.

2. Sea-ice. Accurate wind velocities can not be retrieved from σ_0 measurement if significant ice is formed in the observation area. Sea-ice detection algorithms were used to differentiate ice-covered and ice-free ocean.

Also at present, there is no solid theoretical background to connect wind velocities and σ_0. "Geophysical Model Function" was developed from observations for practical purpose. The output of the GMF is the equivalent neutral-stability wind and conversion of ENW to wind stress produces different results using different algorithms as described in Chapter 1. As a result, the use of SCOW data still needs to be cautious.

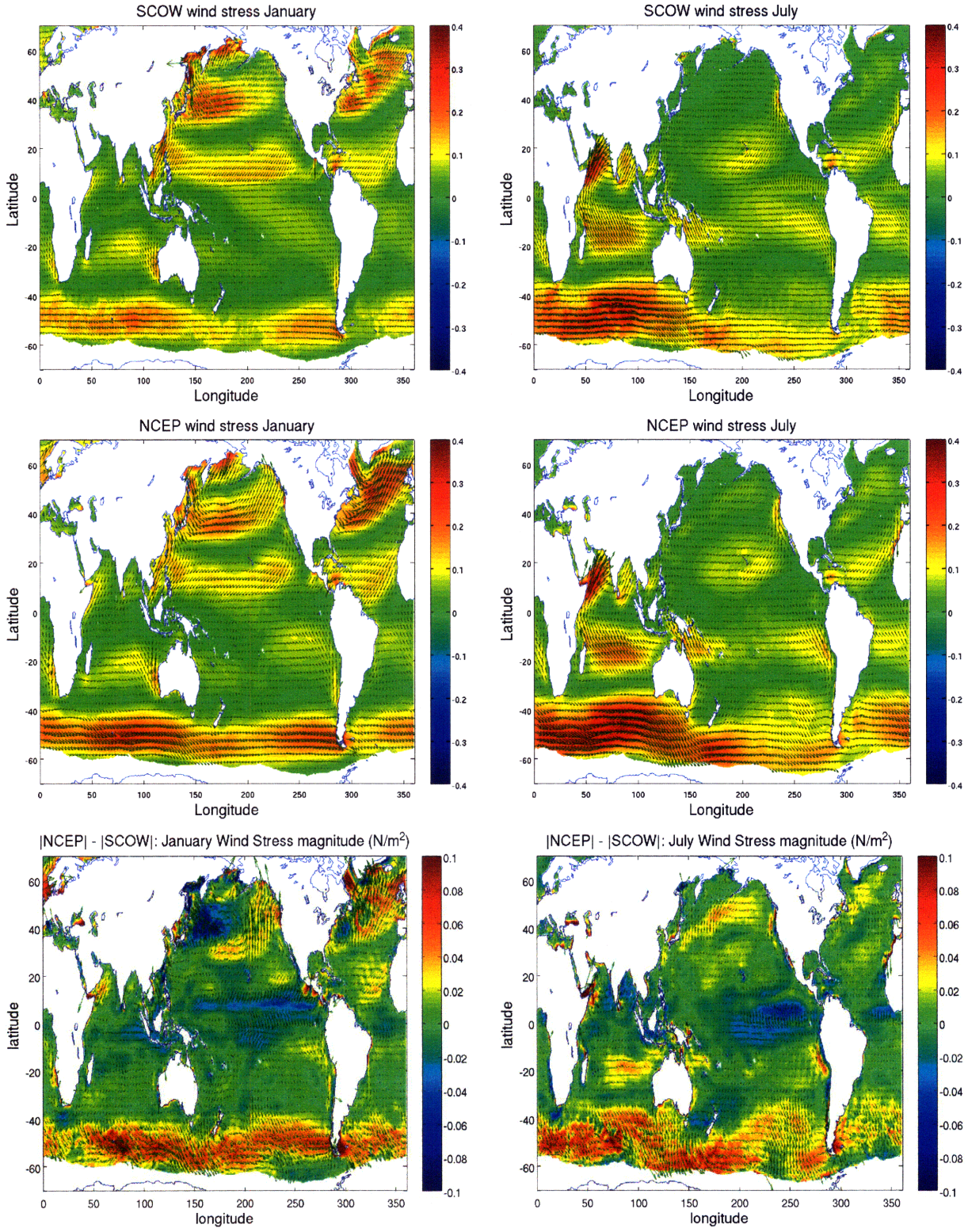

Figure 2.1: The SCOW and NCEP wind stress fields (magnitude and vector) in January and July are displayed respectively. Wind stress vectors are plotted on a coarse 3° × 3° grid for clarity. The bottom panel shows the magnitude difference.

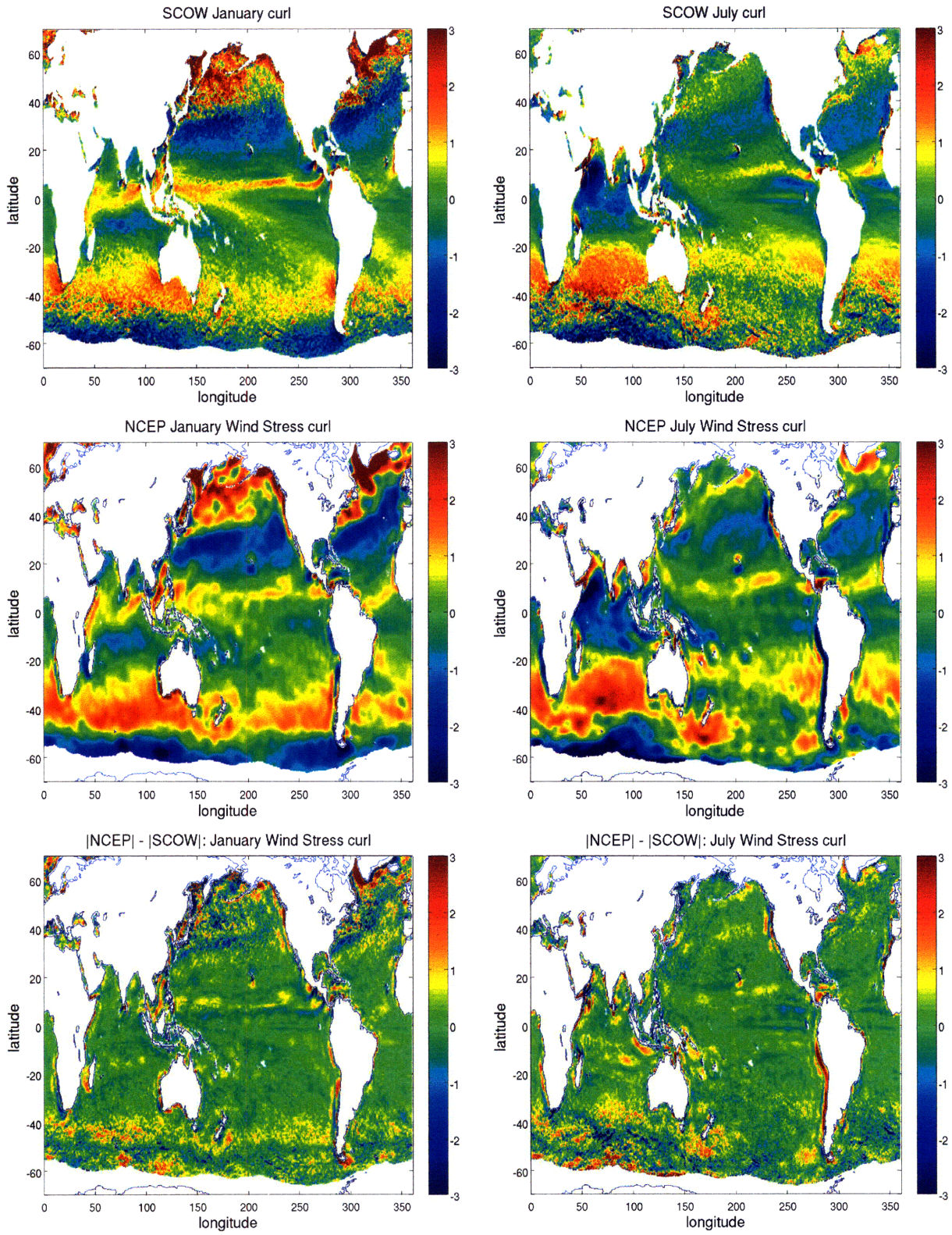

Figure 2.2: Global SCOW/NCEP wind stress curl maps in January and July are shown respectively. The bottom panels display the curl magnitude difference.

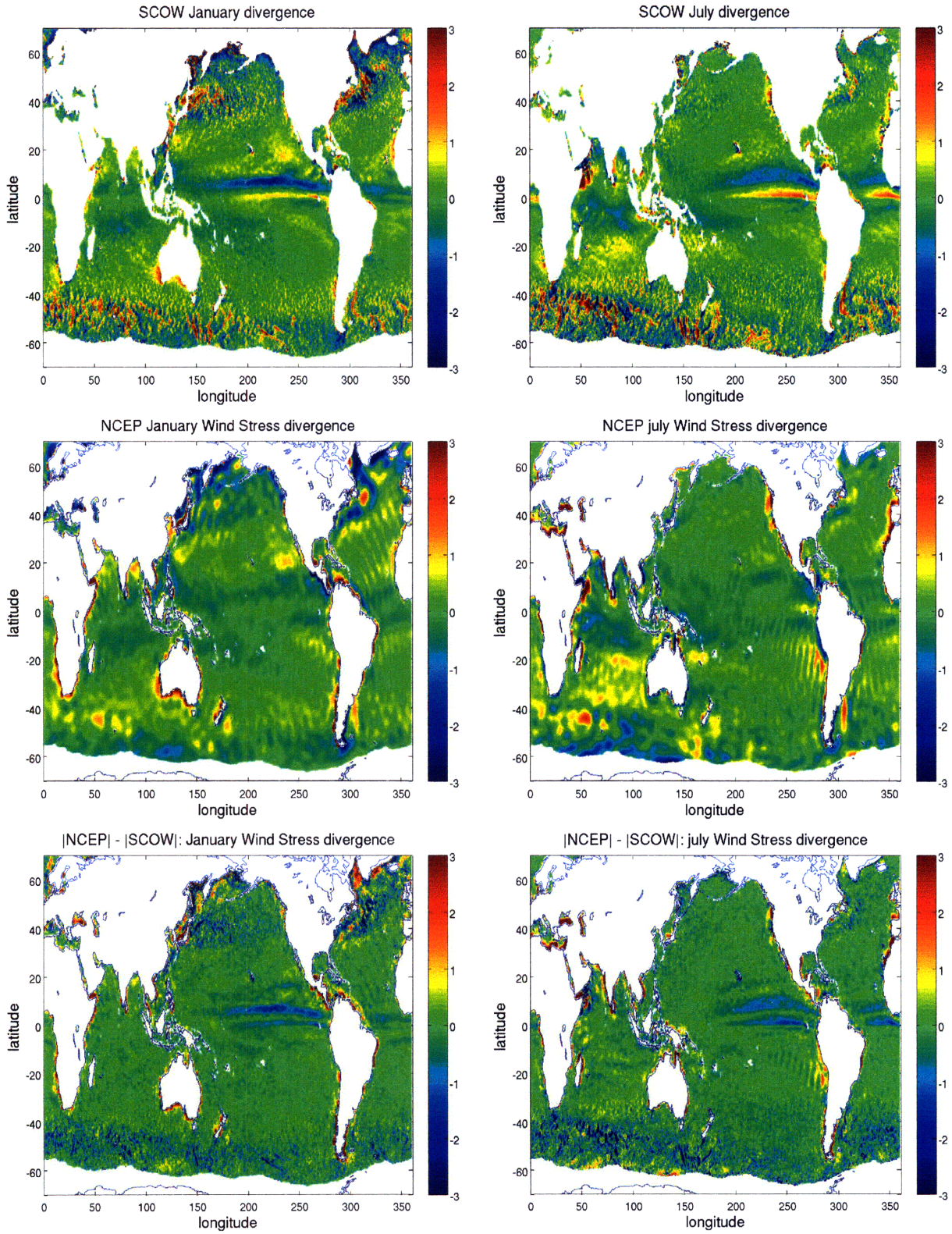

Figure 2.3: Global SCOW/NCEP wind stress divergence maps in January and July are displayed respectively. In middle panels, the NCEP divergence shows strong striping (not sure why). The bottom panel displayed the divergence magnitude difference.

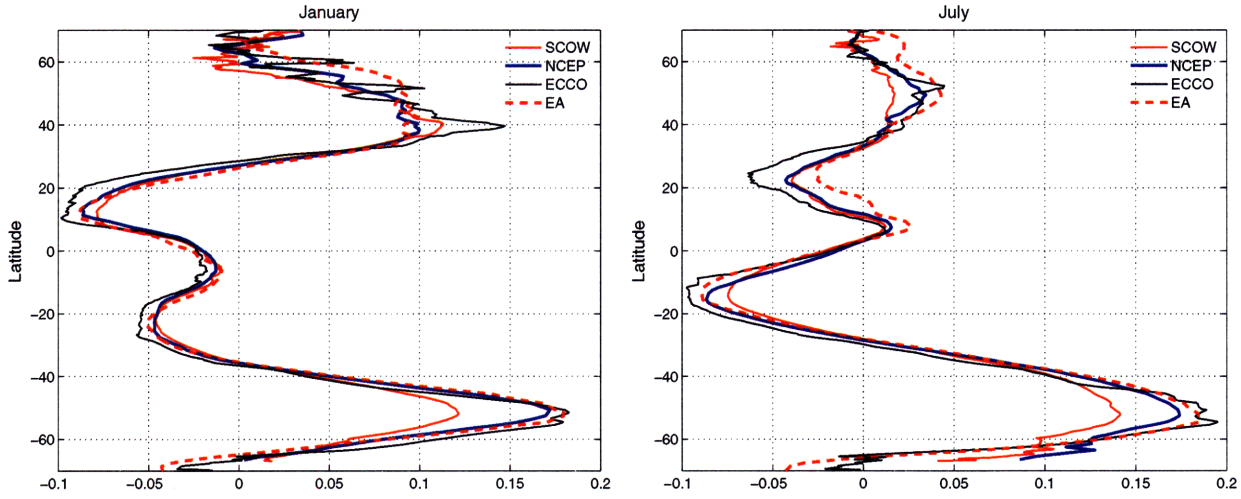

Figure 2.4: Longitudinally averaged zonal stress as a function of latitude for January and July. North of 40N, there are some wiggles on the stress curves. The zonal stress has its maximum at around 50S in the Southern Ocean and it has two minimum at around 12N and 22S.

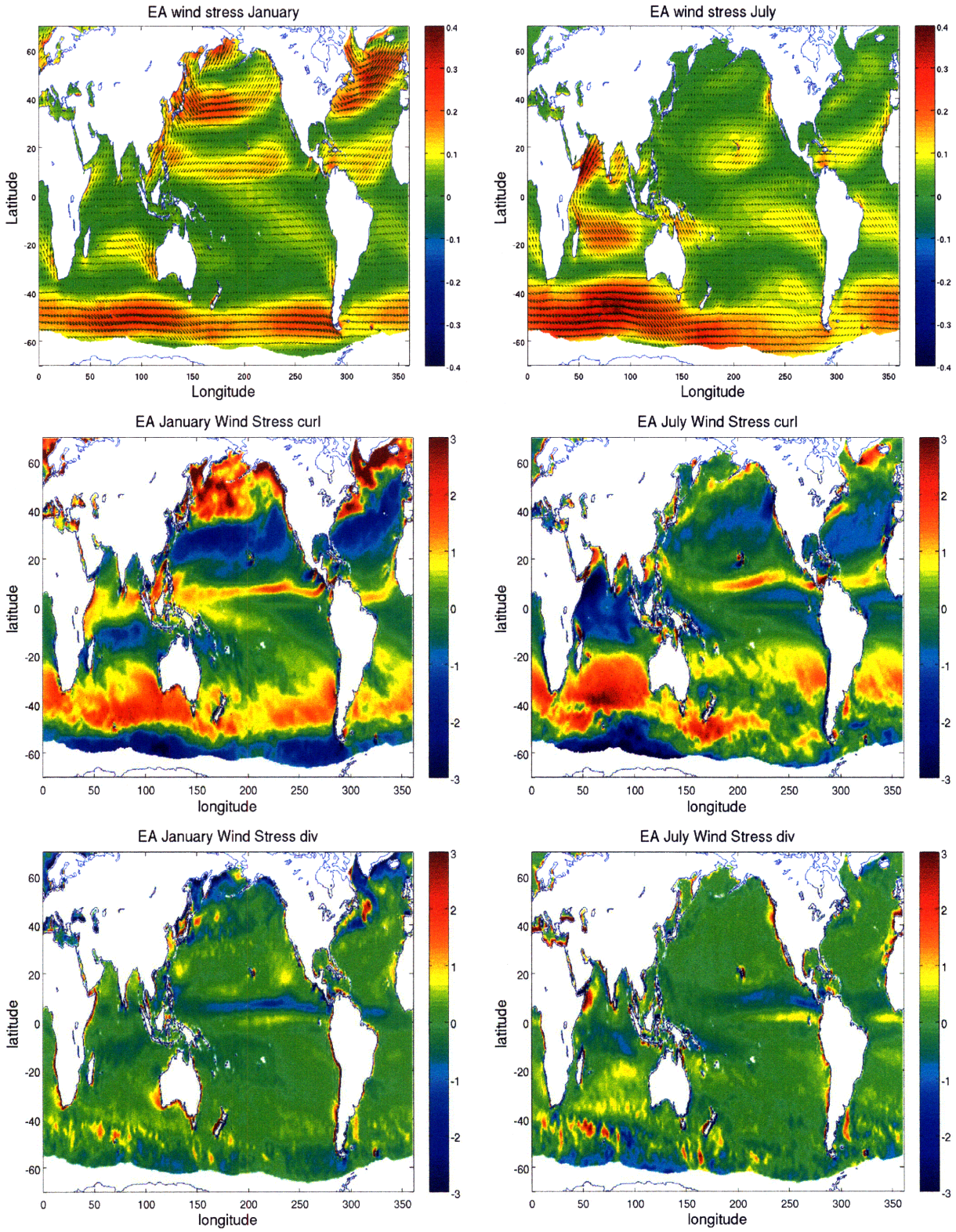

Figure 2.5: ECMWF wind stress maps: stress magnitude (top panels), curl (middle panels), and divergence (bottom panels). Wind stress vectors are plotted on a coarse 3° × 3° grid for clarity.

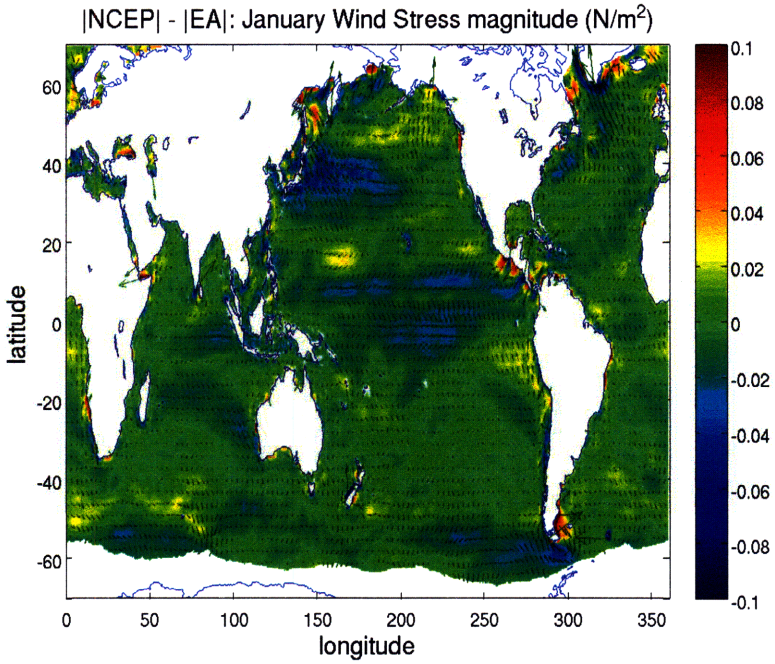

Figure 2.6: Magnitude difference between NCEP and EA data. Wind stress vectors are plotted on a coarse $3° \times 3°$ grid for clarity.

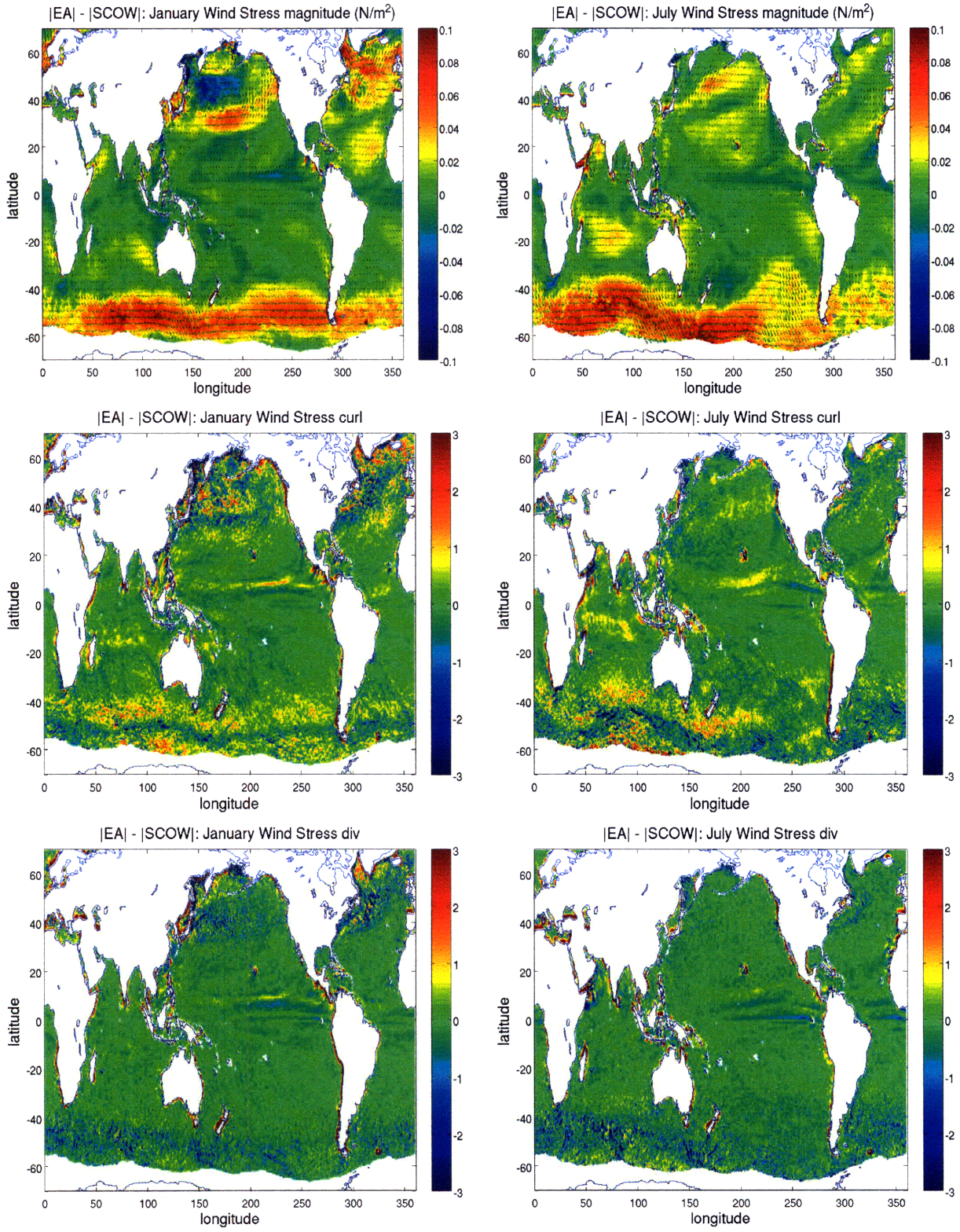

Figure 2.7: ECMWF and SCOW wind stress magnitude difference maps: stress magnitude (top panels), curl (middle panels), and divergence (bottom panels). Wind stress vectors are plotted on a coarse 3° × 3° grid for clarity.

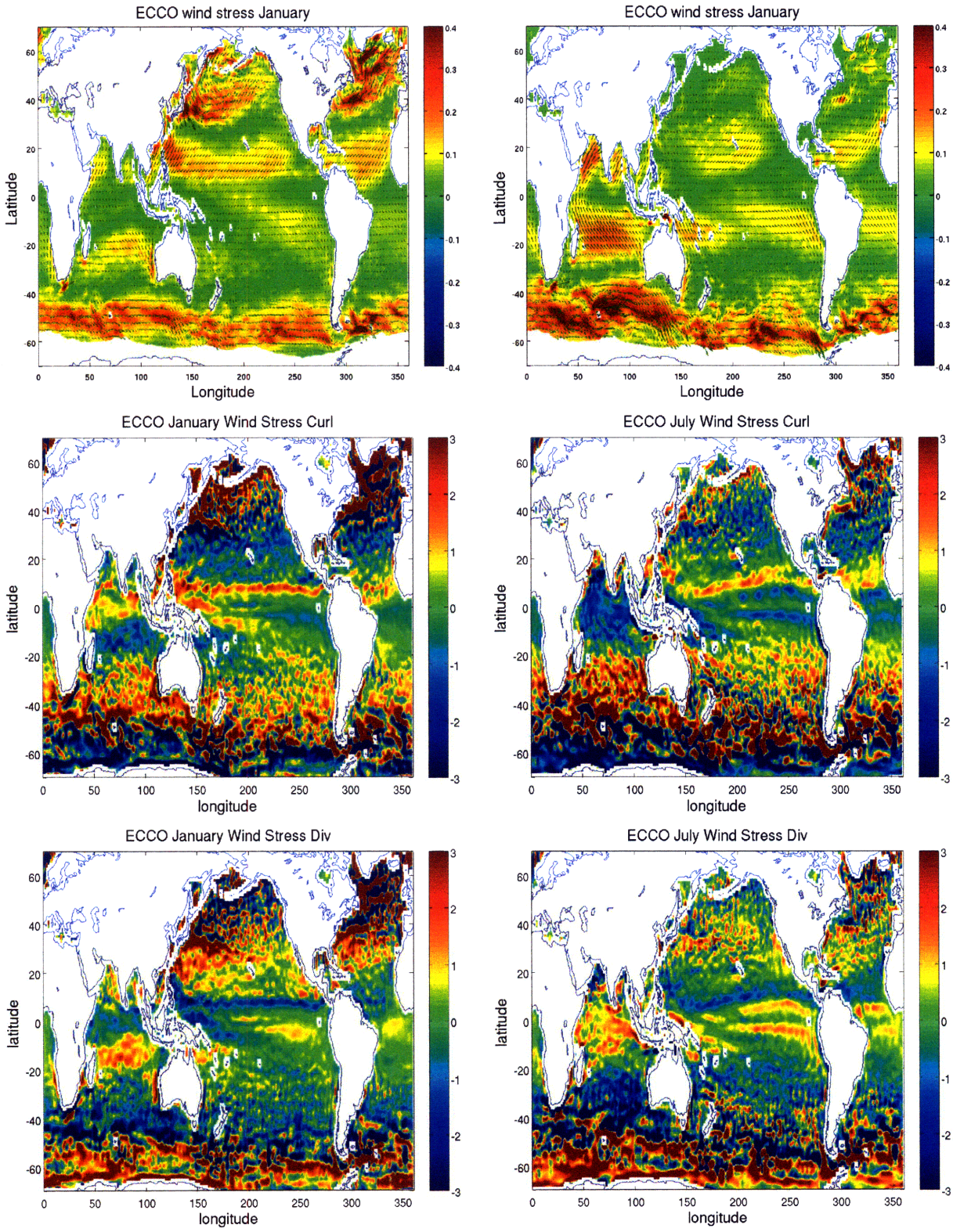

Figure 2.8: ECCO wind stress maps: stress magnitude (top panels), curl (middle panels), and divergence (bottom panels). Wind stress vectors are plotted on a coarse 3° × 3° grid for clarity.

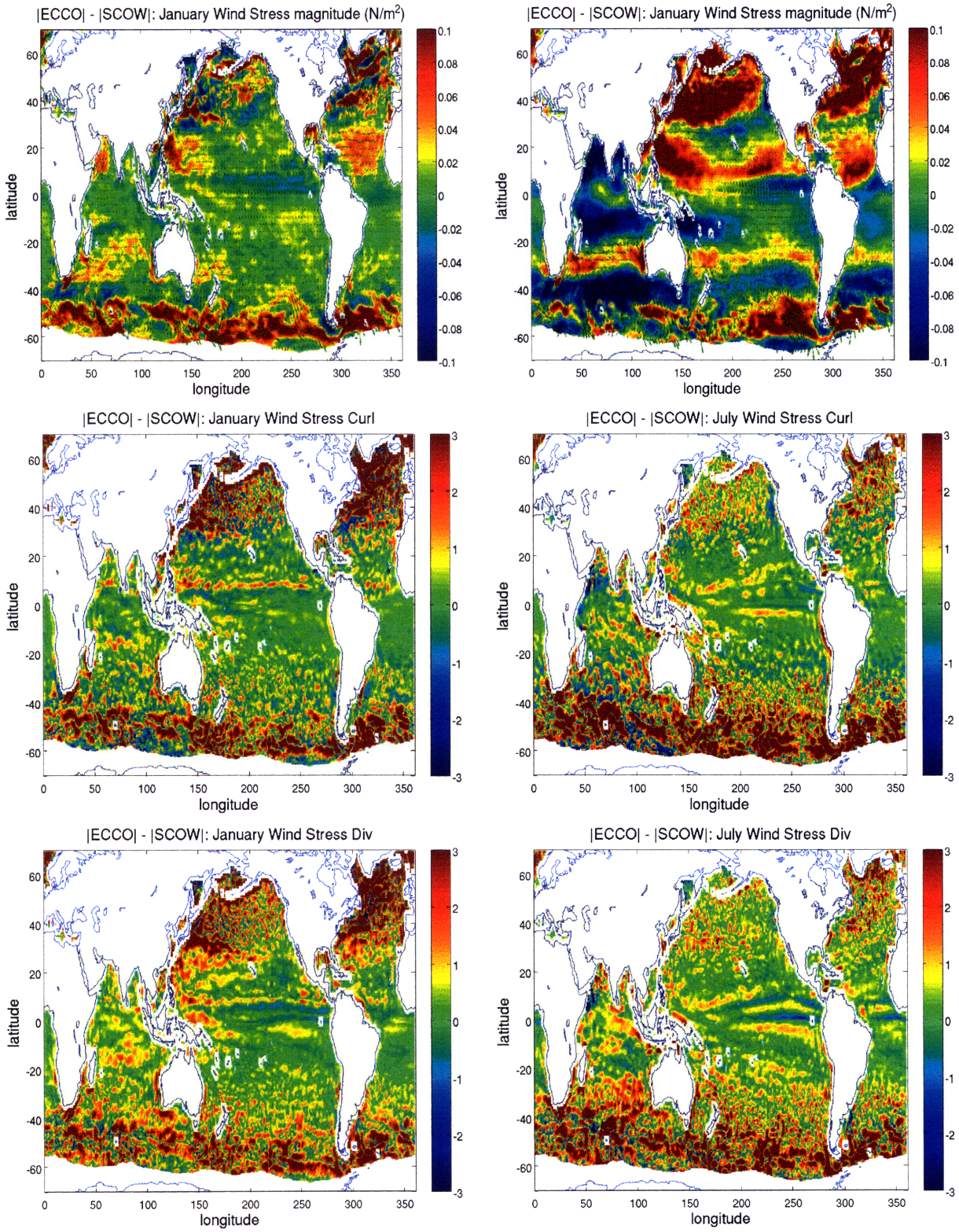

Figure 2.9: ECCO and SCOW wind stress magnitude difference maps: stress magnitude (top panels), curl (middle panels), and divergence (bottom panels). Wind stress vectors are plotted on a coarse 3° × 3° grid for clarity.

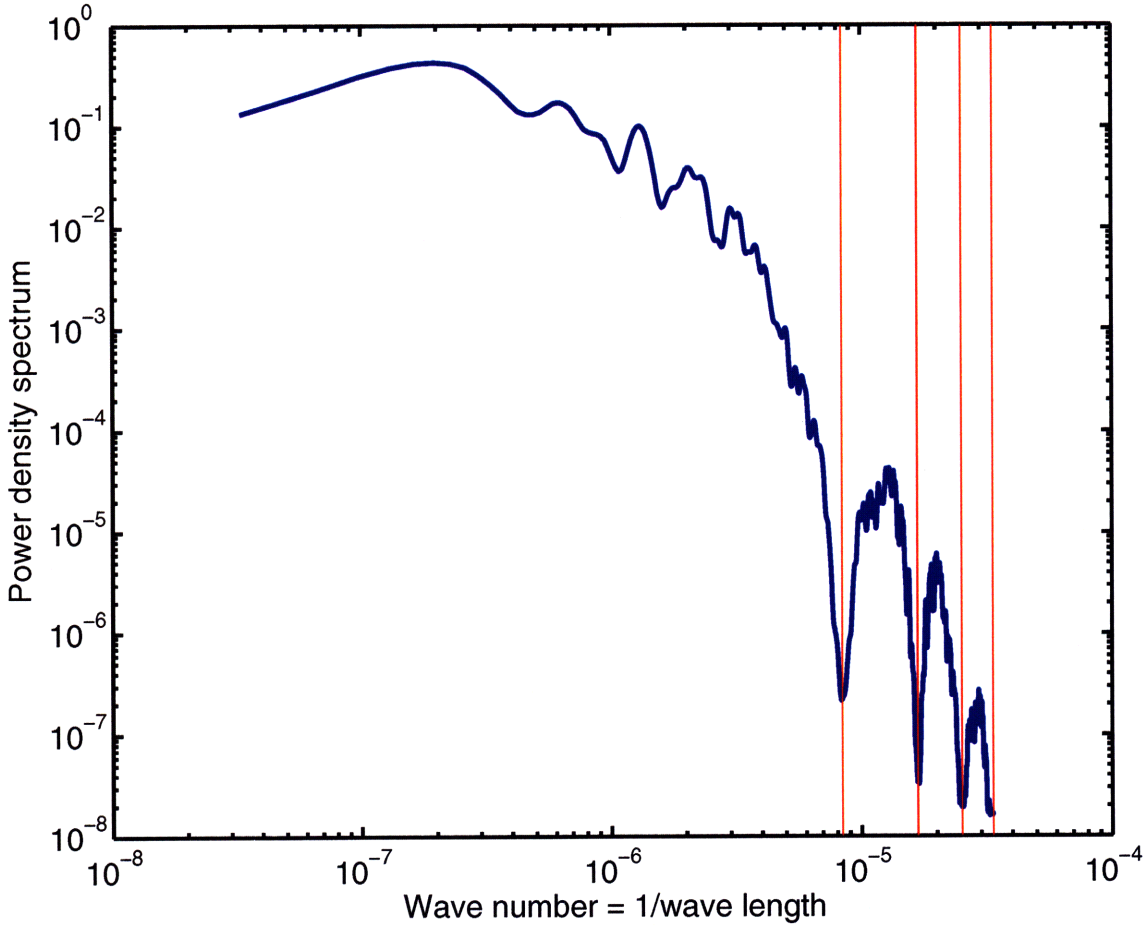

Figure 2.10: Power density spectrum along 57.62°S. The four vertical lines are $2R_L$, R_L, $\frac{2}{3}R_L$, and $\frac{1}{2}R_L$ from left to right, respectively, where $R_L = 2\pi R cos(57.62)/360$=59.54km, and R = 6371km, the Earth Radius.

Chapter 3

Wind Energy Input Reduction

Although the energy input into the ocean itself is an interesting scientific question, the study of the energetics in the ocean circulation has been little discussed over the past years, and only been investigated sporadically until its physical significance on the meridional overturning circulation (MOC) was elaborated by Munk and Wunsch (1998). They pointed out that mechanical energy was required for the maintenance of MOC. they argued that to maintain the density stratification under the present strength of the meridional overturning circulation (MOC), a mechanical energy input of about 2.1TW is required. It was estimated that 0.6-0.9 out of the total 3.7TW from tidal dissipation might be available for abyssal mixing. The question arises as to where the other part of the energy is from?

3.1 Energy input

In Wunsch and Ferrari (2004), the candidates of energy input were determined from the basic equations. They are wind, heating/cooling, evaporation/precipitation, geothermal forcing, and atmospheric loading.

A. Wind

Acting on the ocean surface, winds can directly generate oceanic kinetic energy and potential energy. So far, wind power input (WPI) has been estimated separately according to their individual processes.

$$W_{wind} = \langle \sigma \rangle \cdot \vec{u} = \vec{\tau} \cdot \vec{u}_g + \vec{\tau} \cdot \vec{u}_E + \overline{\vec{\tau}' \vec{u}_0'} + \overline{p' w_0'} \tag{3.1}$$

The first term on the right hand side is the work done by the wind on the geostrophic current. The recent estimate is about 0.8TW, calculated by Wunsch (1998). Because $\vec{\tau} \cdot \vec{u}_g = \vec{U}_{Ek} \cdot \nabla p / \rho$,

it can also be explained as the work done by the Ekman transport against the hydrostatic pressure. Since

$$\langle \vec{\tau} \cdot \vec{u}_g \rangle = \langle \vec{U}_E \cdot \nabla p/\rho \rangle = -\langle w_E p_s/\rho \rangle + \oint \frac{p_s}{\rho} \vec{U}_E \cdot \vec{n} dl, \tag{3.2}$$

it implies that this part of the energy input can be effectively converted into the oceanic potential energy by the work of w against the ambient pressure field, which supports the general ocean circulation.

The second term is the energy input to the Ekman current. The present estimate was estimated by Wang and Huang (2004a) at 2.3-2.4TW. This part of energy input is likely to be used to support and maintain the turbulence and mixing in the Ekman layer. However, the fraction that can be used to support the general ocean circulation is unclear.

Energy input to the inertial motions was estimated by Alford (2003) and Watanabe and Hibiya (2002), using slab models. Although the details of their methods are different, they gave an estimate with only slight difference (0.5 or 0.7TW).

In Wang and Huang (2004b), it is argued that the WPI into the ocean is primarily produced through surface waves. Based on empirical formulas and numerical model results, the number was estimated to be 60TW. Although it appears to be a large number, the contribution of this energy input to the general circulation is not clear.

The fraction of the WPI input, which can penetrate to the abyssal ocean and be used to sustain the MOC, is unknown. However, it is believed that even if it is very small, it, together with the tidal input, is enough to sustain the MOC.

B. Heating/cooling

Using a specific definition of turbulence, Paparella and Young (2002) argued that the horizontal convection (hearting and cooling are at the same geopotential) is nonturbulent in a boussinesq approximation. Recently, Wang and Huang (2005) extended Paparella and Young's result to nonboussinesq fluids. They argued that although the ocean may work as a heat engine (like the atmosphere, although the configuration is different) under the configuration of horizontal convection , the efficiency of the ocean is only 7×10^{-7}, equivalent to a negligible energy input of 1.5×10^{-3}TW compared to the tidal dissipation.

C. evaporation/precipitation and geothermal forcing

Up to now, there is no reliable estimate on the energy input by evaporation and precipitation. The total geothermal heat flux of 32TW produces a rate of heat-to-gravitational-potential-energy about 0.05TW, probably a non-negligible but still small, driving force of the abyssal circulation.

As pointed by Munk and Wunsch, wind energy input constitutes the most important part. In this chapter, our interest is the energy input from the wind stress. However, instead of directly calculating the WPI, we focus on discussing the possible uncertainties associated with the wind stress τ.

3.2 Uncertainties in the WPI

The dot product of wind stress and oceanic surface current velocity defines the wind energy into the surface ocean $W_{wind} = \tau \cdot \vec{u_s}$, where τ is the wind stress and u_s is the oceanic surface velocity (OSV). The bulk formula, $\tau = \rho_a C_D |\vec{U}_a - \vec{u}_s|^2$, is used to calculate the wind stress, where ρ is the atmospheric density, C_D drag coefficient, $\vec{U}_a$ atmospheric velocity and $\vec{u}_s$ OSV.

Because $\vec{u}_s$ is usually much smaller than $\vec{U}_a$, it is traditionally neglected in the formula. However, recent studies show that the introduction of $\vec{u}_s$ into the bulk formula significantly changes the wind energy into the ocean. C_D, as described earlier, is a function of $|\vec{U}_a - \vec{u}_s|$, atmospheric boundary layer stratification, specific humidity, etc. In this section, the atmosphere is assumed neutrally stable, so $C_D = C_D(|\vec{U}_a - \vec{u}_s|)$

Wind stress can be written in the following 4 ways with different choices

$$\vec{\tau} = \rho_a C_D(|\vec{U}_a|)|\cdot \vec{U}_a| \cdot \vec{U}_a \tag{3.3a}$$

$$\vec{\tau} = \rho_a C_D(|\vec{U}_a|) \cdot |\vec{U}_a - \vec{u}_s| \cdot (\vec{U}_a - \vec{u}_s) \tag{3.3b}$$

$$\vec{\tau} = \rho_a C_D(|\vec{U}_a - \vec{u}_s|) \cdot |\vec{U}_a - \vec{u}_s| \cdot (\vec{U}_a - \vec{u}_s) \tag{3.3c}$$

$$\vec{\tau} = \rho_a C_D(|\vec{U}_a - \vec{u}_s|) \cdot |\vec{U}_a| \cdot \vec{U}_a \tag{3.3d}$$

Eq. (3.3a) is the traditional wind stress definition; Eq. (3.3b) introduces the OSV in the square term, but neglects the drag coefficient dependence, which is generally assumed in recent studies (Xu and Scott, 2008); Eq. (3.3c) further includes the C_D dependence; the last one (3.3d) only has the dependence in the C_D term to isolate how this term will change the energy input.

A simple numerical computation

Now it is widely acknowledged that accounting for an OSV in the bulk formula leads to a significant reduction of the WPI to the ocean general circulation by around 17-35%. The presence of oceanic mesoscale eddies enhances the dissipation rate at the air-sea interface and reduces the WPI as illustrated by Xu and Scott, 2008 (Fig. 5). Above an oceanic eddy, if the OSV is in the same/opposite direction as the wind velocity, the wind stress is reduced/enhanced by including the OSV, and so does the positive/negative WPI. This explains why the oceanic eddies, either cyclonic or anticyclonic, serve as damping machines.

Here a simple example numerical experiment was carried out. There is an eddy in an infinitely large zonal flow $u_0 = 0.01m/s$. The eddy velocity field is written as

$$1000C_H = \begin{cases} u_{meso} = \dfrac{r}{R_0}V \\ u_{meso} = \dfrac{R_0}{r}V \end{cases} \tag{3.4}$$

where $R_0 = 50km$ and $V = 0.25m/s$. The size of the eddy is defined as the e-folding scale of V. The atmospheric velocity is set to $U_s = 10m/s$.

Fig. 3.1 displayed the surface velocity vector map. It is readily seen that the circle is distorted a little bit by the zonal flow. The edge of the eddy is defined by the e-folding scale (red line). All the following computations are confined to this region. In the computation, the atmosphere is assumed neutrally stable and the LT96 algorithm is applied.

The WPI maps, computed from Eqs. (3.3a) and (3.3c), are shown in Fig. (3.2a, b) share similar features. When the wind velocity is in the same/opposite direction as the OSV, the WPI is positive/negative. In Fig. 3.2a, the positive WPI is stronger than that in Fig. 3.2b; the negative WPI is weaker than that in Fig. 3.2b.

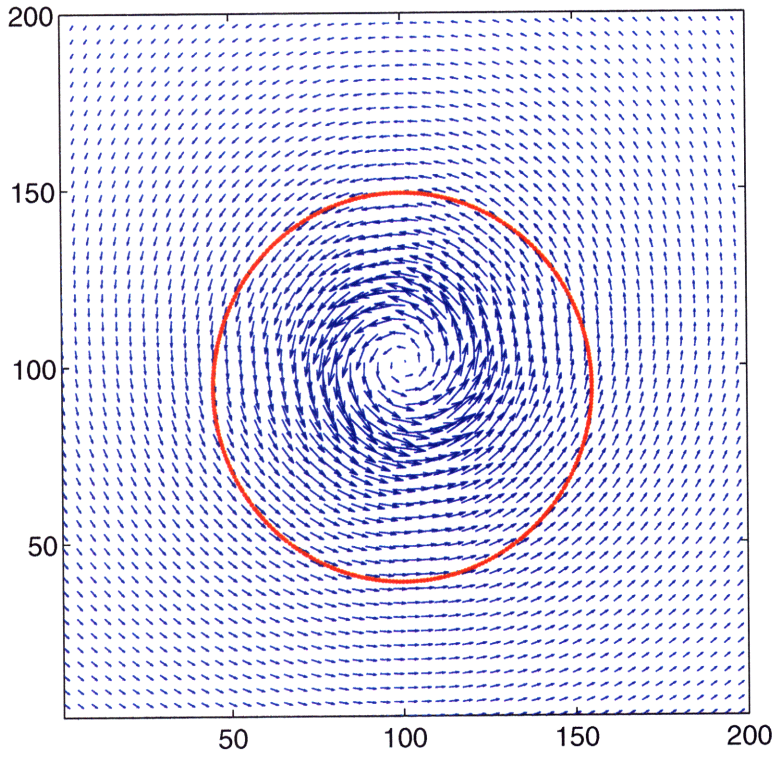

Figure 3.1: The eddy field defined by Eq. 3.4. The grid unit is km

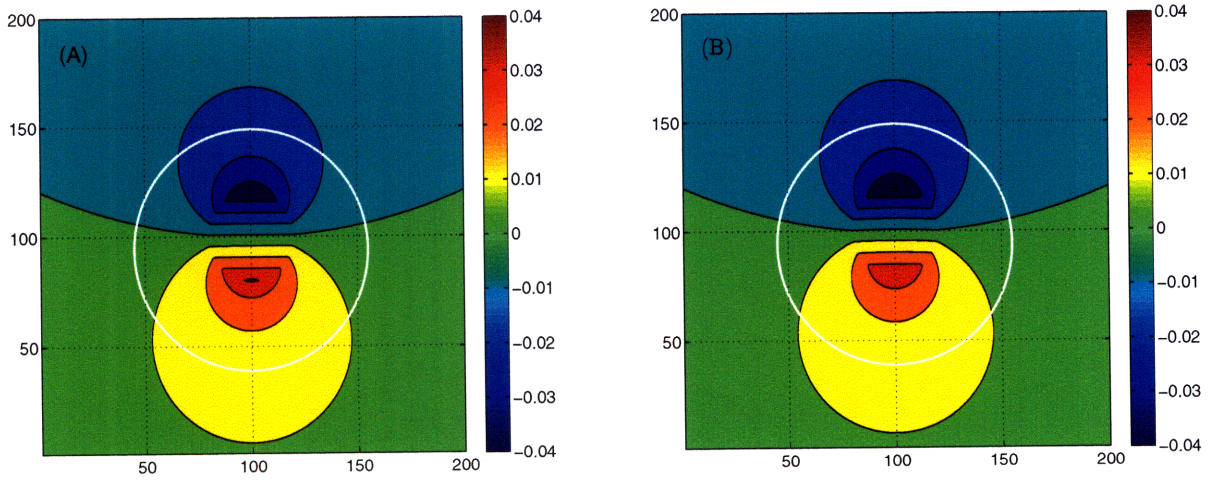

Figure 3.2: The WPI computed from Eq. (3.3a) (A) and Eq. (3.3c) (B). The two maps share similar features, but the WPI in (A) is everywhere bigger than (B). The grid unit is km.

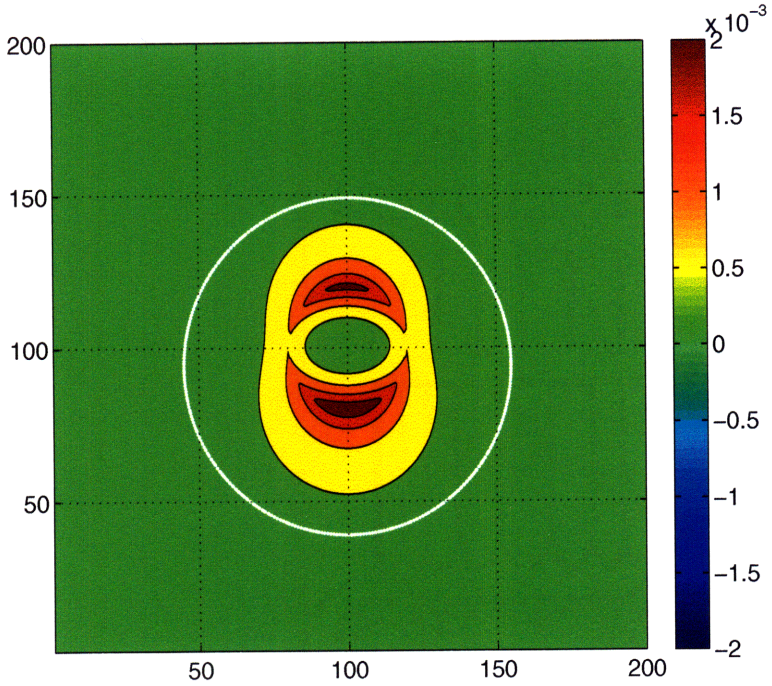

Figure 3.3: The difference of WPI computed from Eq. (3.3a) (A) and Eq. (3.3c) (B) and the difference is positive definite. The grid unit is km.

Evidently, the difference is positive definite as shown in Fig. 3.3. The maximum difference occurs where the eddy has maximum zonal velocity as expected. The map is not symmetric about $y = 100$ because $u_0 \neq 0$.

This has been demonstrated in many studies (Xu and Scott, 2008; Hughes and Wilson, 2008). Here the focus on the uncertainties associated with different choices of wind stress. The mean WPI into the eddy for Eqs. (3.3a, 3.3b, 3.3c, 3.3d) are 3.14×10^{-3}, 2.64×10^{-3}, 2.57×10^{-3}, and 3.07×10^{-3} Wm^{-2}, respectively. The corresponding reduction ratio is around 19%, 22%, 2%. The introduction of the OSV dependence in the drag coefficient leads to a small reduction of a little more than 2%. However, the reduction rate from around 19% to 22% indicates an average decrease of about 17% relative to Eq. 3.3b. Under this experiment configuration, the presence of the OSV dependence in both terms provides the most significant reduction of the WPI. In the computation of the WPI, the OSV dependence in the drag coefficient can not be neglected although the dependence in the square term dominates.

As discussed in Chapter 1, the use of different algorithms results in different WPI. For this idealized numerical experiment, the ECMWF algorithm yields a WPI, roughly 20% (ref.

Chapter 1) stronger than the WPI produced by LY04 algorithm (details are not included, but the result can in inferred from the last figure in Chapter 1). Now the important conclusion is that the use of different algorithms may produce uncertainties as large as those resulting from the inclusion of the OSV dependence in the algorithms.

3.3 The WPI computed from ECCO data

The idealized numerical experiment gives some preliminary results on the WPI. However, the atmosphere is not absolutely in neutral-stability conditions and there are much more than one eddy in the ocean. A computation based on the "real" oceanic data is executed here.

The data used here is from the ECCO group. The data span in the Southern Ocean with a high spatial resolution of $1/6° \times 1/6°$ (Mazloff, 2008). For those who are more interested in the data, here is the website: http://www.ecco-group.org.

From the estimate by Wunsch (1998), Wang and Huang (2004a, 2004b), Xu and Scott (2008), etc, the WPI in the Southern Ocean dominates the energy input into the world ocean. Also the Southern Ocean is full of energetic eddies, cyclonic or anticyclonic. Accordingly, the Southern Ocean becomes a very interesting region to test the differences associated with the inclusion of OSV in the bulk formula and the use of different algorithms.

For the time being, we focus the difference resulting from the use of different algorithms and in the computation, the OSV dependence is neglect. Time evolution of C_D for two randomly selected points is shown in Fig. 3.4. LY04, UA and ECMWF algorithms are applied to compute the corresponding C_D. As predicted from the neutrally stable conditions, the ECMWF algorithm generally produces the largest C_D, while LY04 yields the smallest. There are a few exception points at which the LY04 drag coefficients are much larger due to the nature that when the wind speed approaches zero, C_D tends to be infinitely large.

Associated with the C_D difference, different stresses are produced and the corresponding WPI are surely different. The WPI corresponding to the three algorithms are show in Fig. 3.5 for the year of 2001. It is readily seen that the WPI computed from the ECMWF algorithm is only slightly larger than that from UA algorithm, but they both are significantly larger than that from the LY04 algorithm as expected. The mean WPI for ECMWF, UA and LY04

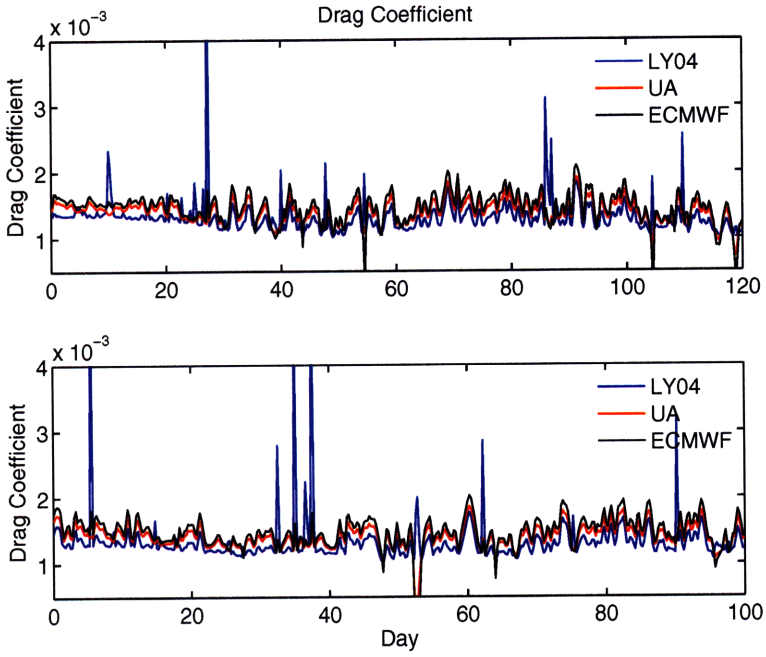

Figure 3.4: Time evolution of C_D as a function of time for two randomly selected points.

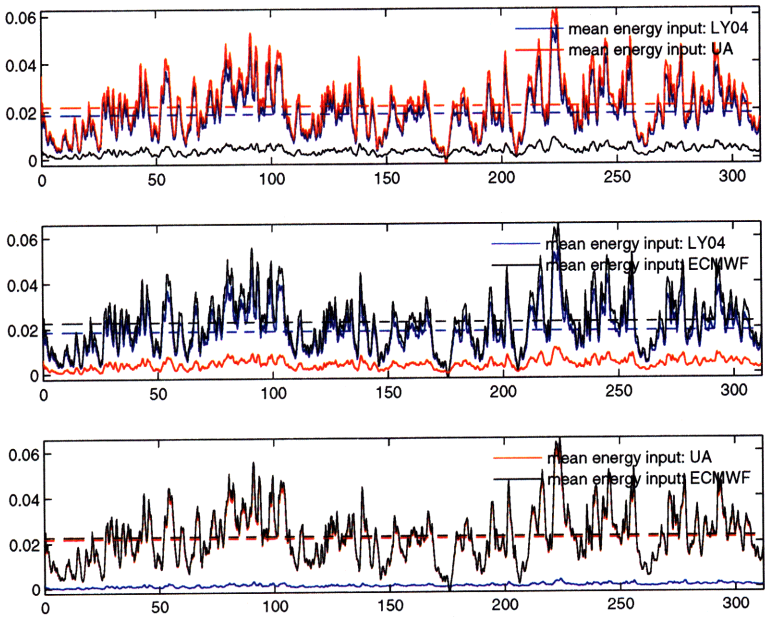

Figure 3.5: The **WPI** computed from LY04, UA and ECMWF algorithms as a function of time. The horizontal lines are the corresponding mean values.

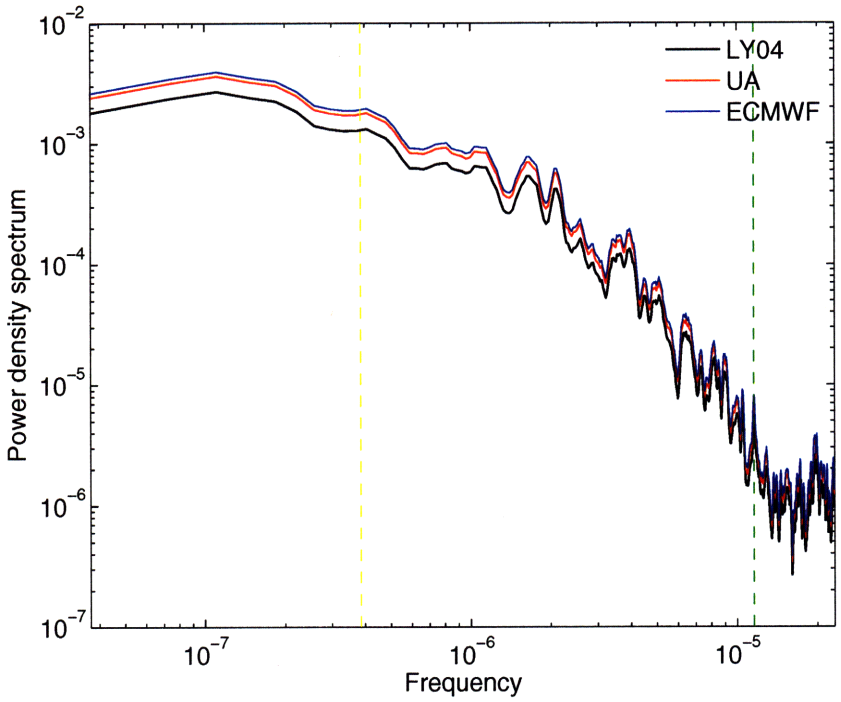

Figure 3.6: The power density spectrum of the WPI computed from LY04, UA and ECMWF algorithms as a function of time. The frequency unit is s^{-1}.

algorithms are about 23×10^{-3}, 22×10^{-3} and 19×10^{-3}, respectively. The ECMWF algorithm generates a WPI, which is around 21% stronger than that from LY04 algorithm.

Fig. 3.6 displays the corresponding power spectrum. A diurnal cycle (frequency=$1.16 \times 10^{-5}\text{s}^{-1}$) is observed in the WPI . Around 65% of the WPI is in the timescale between 1 day and 30 days.

The use of different algorithms results in significantly different WPI. The previous analysis also indicates a significant different WPI with the presence of the OSV dependence in the computation of wind stress. However, using the ECCO data, we do not find significant difference with or without the OSV dependence as shown in Fig. 3.7. The WPI without inclusion of the OSV dependence is only slightly larger than that without the dependence (22.64×10^{-3} versus $21.47 \times 10^{-3}\text{Wm}^{-2}$). Actually, the ECCO wind velocity (not stress), to a great extent, is the adjusted NCEP wind velocity with oceanic information included. In other words, the ECCO wind differs from the wind which produces the ECCO oceanic surface velocity. As a result, including the OSV in the wind stress computation does not leads to a significant reduction of

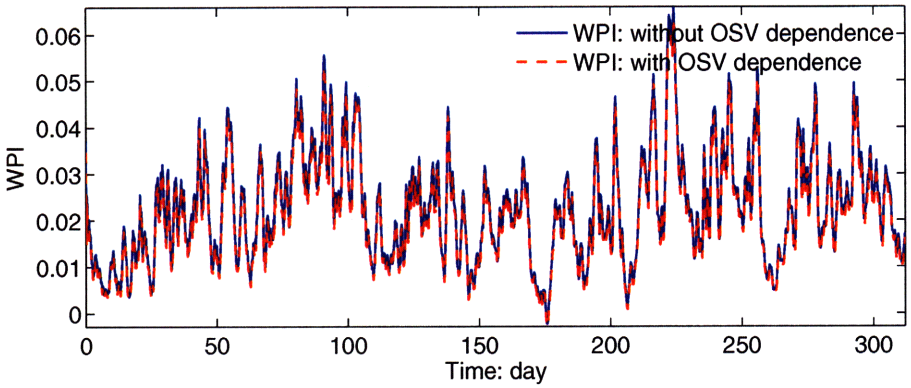

Figure 3.7: The difference of WPI computed from ECMWF algorithm with and without the *OSV* dependence.

the WPI.

One speculation is that since the SCOW data are the best wind stress dataset available, the oceanic model driven by the SCOW data will yield the best estimate of the WPI into the world ocean. From the above analysis, it is concluded that this is not true. First, the SCOW wind stress already contains the OSV information; second, the oceanic model represents a chaotic system and the produced oceanic states driven by the SCOW data differ from the oceanic information contained in the SCOW data. Xu and Scott (2008) did an interesting calculation. Since the SCOW wind are essentially $\vec{U}_a - \vec{u}_s$, the sum of the SCOW wind and the OSV $\vec{u}_s$ produces the net atmospheric velocity $\vec{U}_a$. Using the SCOW wind stress data and the surface current data from AVISO gridded merged product of absolute geostrophic velocity compiled by the CLS Space Oceanographic division of Toulouse (France), the global integrals of 6-year mean WPI with and without OSV dependence are 0.91TW and 1.20TW, which indicates a WPI reduction rate of 32%.

3.4 Summary

The wind stress dependence on the OSV in the bulk formula has long been neglected because the OSV magnitude is much smaller than the atmospheric speed magnitude. With the recognition of the importance of the energy input (especially WPI) into the oceanic circulation, oceanographers begin to realize although the presence of the OSV in the computation of the

drag coefficient and wind stress changes the wind stress only slightly, it leads to significant decrease of the WPI into the world ocean. The difference comes from the oceanic eddy damping effects as discussed above. The numerous eddies in the ocean, cyclonic and anticyclonic, reduces the WPI in a way that if the OSV is in the same/opposite direction as the atmospheric velocity, the positive/negative WPI is decreased/increased.

The nature of the ocean system is chaotic. No matter how good the model is and no matter how accurate the initial conditions are, the model results will deviate exponentially from the real states. With the constraints of simultaneous observations, the model may mimic the large scale circulation well, but the smaller scale (e.g. mesoscale) motions are less well simulated. However, the WPI reduction is mainly associated with the mesoscale eddies. If the mesocale eddies are not well simulated, the WPI reduction rate due to the OSV may not be significant, and that is one reason why the reduction rate from ECCO data is small.

The essence of the ECCO project to use as many data as possible, along with models, to produce the best atmospheric and oceanic estimate. As a result, the produced wind data contain the oceanic information, which is another reason why the introduction of OSV does not reduce the WPI significantly for ECCO wind data.

The WPI reduction rate is significant only when the OSV contained in the wind stress matchs the corresponding OSV. If the oceanic models are forced directly by the SCOW data, the computed WPI reduction rate may not be significant just because the simulated OSV differs from the OSV information contained in the SCOW data. As a result, direct application of the SCOW data to force the oceanic general circulation models needs to be cautious.

The use of different bulk algorithms to compute wind stress also yields significant difference in WPI. Generally speaking, among the algorithms discussed here, the wind stress computed from LY04 is around 20% weaker than that from the ECMWF algorithm, and the corresponding WPI is accordingly weaker. Conversion of atmospheric velocity to wind stress as accurate as possible is essential to quantify the WPI into the world ocean.

Acknowledgements

Although this is only a master thesis, my thesis advisor, Professor Carl Wunsch, gave me all the opportunities he has to allow me to finish it. Without his support, it is not possible to have the thesis available. Also the department and MIT-WHOI joint program are also greatly appreciated in helping me in fixing all different problems.

Being a joint program student is a great experience, and it's a great pleasure to be in the office 54-1511A. To some extent, I has been struggling along the road, and now it's time to have something.

This work was supported in part by the National Ocean Partnership Program (NASA, NSF), which is also appreciated.

References

[1] Alford, M. H., 2003. Improved global maps and 54-year history of wind-work on ocean inertial motions. *Geophys. Res. Lett.,* 30, 1424, doi:10.1029/2002GL016614.

[2] Beljaars, A., 1994. The parametrization of surface fluxes in large-scale models under free convection. *Q. J. R. Meteorol. Soc.,* 121, 255-270.

[3] Brunke, M., *et al.,* 2003. Which bulk aerodynamic algorithms are least problematic in computing ocean surface turbulent fluxes? *J Climate,* 16, 619-635.

[4] Brutsaert, W., 1982. Evaporation into the atmosphere. reidel, 299pp.

[5] Chelton, D. B., *et al.*, 2004. Satellite measurements reveal persistent small-scale features in ocean winds. *Science,*, 303, 978-983.

[6] Chelton, D. and M. H. Freilich, 2005. Scatterometer-based assessment of 10-m wind analyses from the operational ECMWF and NCEP numerical weather prediction models. *Mon. Wea. Rev.,* 133, 409429.

[7] Dawe, J. and L. Thompson, 2001. Effect of ocean surface currents on wind stress, heat flux, and wind power input to the ocean. *Geophys. Res. Lett.,* 33, L09604, doi:10.1029/2006GL025784.

[8] Duhaut, T. and D. Straub, 2006. Wind stress dependence on ocean surface velocity: Implications for mechanical energy input to ocean circulation. *J. Phys. Oceanogr.,* 36, 202-211.

[9] Foken, T., 2006. 50 years of the Monin-Obukhov similarity theory. *Boundary-Layer Meteorol.* 119, 431-447.

[10] Hogstrom, U., 1988. Non-dimensional wind and temperature profiles in the atmospheric surface layer: A re-evaluation. *Boundary Layer Meteorol.*, 42, 55-78.

[11] Hughes, C. and C. Wilson, 2008. Wind work on the geostrophic ocean circulation: An observational study of the effect of small scales in the wind stress. *J. Geophys. Res.,* 113, C02016, doi:10.1029/2007JC004371.

[12] Large, W. and S. Yeager, 2004. Diurnal to decadal global forcing for ocean and sea-ice models: The data sets and flux climatologies. *Technical Report TN-460+STR*, NCAR, 105pp.

[13] Liu, W. and W. Tang, 1996. Equivalent neutral wind. *JPL Publication* 96-17, Jet Propulsion Laboratory, Pasadena, 16pp.

[14] Mazloff, M., 2008. The southern ocean eridional overturning circulation as diagnosed from an eddy permitting state estimate. Ph.D thsis, MIT-WHOI joint program.

[15] Munk, W. and C. Wunsch, 1998. The moon and mixing: abyssal recipes 2. *Deep-Sea Res.,* 45A, 1977-2010.

[16] Naderi, F., M.H. Freilich, and D.G. Long, 1991. Spaceborne radar measurement of wind velocity over the ocean - an overview of the NSCAT scatterometer system. *Proceedings of the IEEE*, 79(6), 850-866.

[17] Paparella, F. and W. R. Young, 2002. Horizontal convection is non-turbulent. *J. Fluid Mech.,* 466, 205-214.

[18] Paulson, C. A., 1970. the mathematical representation of wind speed and temperature profile in the unstable atmospheric surface layer. *J. Appl. Meteorol.,* 9, 857-861.

[19] Risien, C. and D. Chelton, 2008. A global climatology of surface wind and wind stress fields from 8 years of QuikSCAT scatterometer data. *J. Phys. Oceanogr.,* in press.

[20] Stewart, R. Introduction to physical oceanography. online version, 345pp

[21] Wang, B., *et al.,* 1999. Roles of the western North Pacific wind variation in thermocline adjustment and ENSO phase transition. *J. Meteor. Soc. Japan,* 77, 1-16.

[22] Wang, W. and R. X. Huang, 2004a. Wind energy input to the Ekman layer. *J. Phys. Oceanogr.,* 34, 1267-1275.

[23] Wang, W. and R. X. Huang, 2004b. Wind energy input to the surface waves. *J. Phys. Oceanogr.,* 34, 1276-1280.

[24] Wunsch, C., 1998. The work done by the wind on the oceanic general circulation *J. Phys. Oceanogr.,* 28, 2332-2340.

[25] Wunsch, C. and R. Ferrari, 2004. Vertical mixing, energy, and the general circulation of the oceans. *Ann. Revs. Fl. Mech.,* 36, doi:10.1146/annurev.fluid.36.050802.122121.

[26] Wunsch, C. and P. Heimbach, 2007. Practical Global Oceanic State Estimation. *Physica D,* 230, 197-208.

[27] Xu, Y. and B. Scott, 2008. Subtleties in forcing eddy resolving ocean models with ssatellite wind data. *Ocean Modeling,* 20, 240251

[28] Zeng, X. *et al.,* 1998. Intercomparison of bulk aerodynamic algorithms for the computation of sea surface fluxes using TOGA COARSE and TAO data. *J. Climate,* 11, 2628-2644.